A novel 2D diffusion model for composite domain with non-regularly shaped interface

William Dumontaud, Julien Berger, Benjamin Kadoch

Contents lists available at ScienceDirect

Computers and Mathematics with Applications

journal homepage: www.elsevier.com/locate/camwa

A novel 2D diffusion model for composite domain with non-regularly shaped interface

William Dumontaud [a,*], Julien Berger [a], Benjamin Kadoch [b]

[a] Laboratoire des Sciences de l'Ingénieur pour l'Environnement (LaSIE), UMR 7356 CNRS, La Rochelle Université, CNRS, La Rochelle, 17000, France
[b] Institut Universitaire des Systèmes Thermiques Industriels (IUSTI), UMR 6595 CNRS, Aix-Marseille Université, Marseille, 13013, France

ARTICLE INFO

Keywords:
Two-dimensional diffusion
Numerical model
Interface problem
Ghost fluid method
DuFort-Frankel scheme

ABSTRACT

This paper presents a new two-dimensional transient diffusion model adapted to composite domains with non-regular internal interfaces. The model employs a finite difference approach based on the explicit DuFort–Frankel scheme, coupled with the Ghost Fluid Method, to ensure both numerical efficiency and accurate interface treatment. Discontinuities in field values and fluxes across subdomains are captured using mesh-aligned directional approximations, allowing the computation to remain on a regular Cartesian grid.

The numerical scheme is first validated against an analytical solution, demonstrating second-order accuracy in both space and time. Additional validation is performed through comparison with a finite element model under realistic thermal boundary conditions relevant to building physics.

The model is subsequently applied to the optimization of the interface geometry between two materials in a building wall, exposed to spatially heterogeneous conditions typical of an urban canyon environment. Thermal performance is assessed using two distinct cost functions. Although the average improvements over annual and monthly timescales are moderate, the model identifies significant instantaneous performance gains at the hourly scale.

1. Introduction

Accurately modeling transient diffusion processes in heterogeneous domains with internal discontinuities is a longstanding challenge in computational mathematics and physics. Many classical formulations rely on structured, layered configurations where transitions between regions are treated as piece wise homogeneous by simply changing the physical properties [1], or by matching diffusivity [2]. Such assumptions are often sufficient for global assessments in domains with regular structure, such as in current building walls [3] or simplified composite barriers, but tend to oversimplify the interfacial behavior.

However, in many applied contexts, domain configurations become increasingly complex, characterized by embedded interfaces, spatially localized sources, or irregular internal layouts. A wide range of engineering disciplines have therefore developed advanced computational models to address the topological and interfacial complexities inherent in such multiphysics systems. In fields such as fluid and solid mechanics, numerical frameworks have been designed to represent heterogeneous domains with evolving or irregular internal structures, often involving sharp thermal [4], mechanical [5], chemicals [6], or phase discontinuities [7]. Accurately capturing the physical behavior in these cases often requires resolving strong gradients and jump conditions at irregular interfaces, which

* Corresponding author.
E-mail address: william.dumontaud@ens-paris-saclay.fr (W. Dumontaud).

https://doi.org/10.1016/j.camwa.2026.06.007
Received 30 June 2025; Received in revised form 16 April 2026; Accepted 10 June 2026

Nomenclature

Latin letters

a	temperature jump [K]
b	flux jump [W.m^{-2}]
Bi	BIOT number [−]
c	volumetric heat capacity [J.m^{3}.K^{-1}]
$\mathcal{C}$	cost function [J]
f	source term [W.m^{-3}]
Fo	FOURIER number [−]
h	shadow height [m]
h, h_{10}, h_{11}, h_{20}, h_{21}	surface heat transfer coefficient [W.m^{-2}.K^{-1}]
H_0, H_1	vertical limit of the domain [m]
H	building facade height [m]
L_0, L_1	horizontal limit of the domain [m]
L	wall length [m]
N_p, N_t, N_x, N_y	number of elements [−]
$\mathbf{p}$	interface parameters [−]
q	thermal flux [W.m^{-2}]
t, t_f	time [s]
T	temperature [K]
u	dimensionless temperature [−]
v_∞	wind velocity [m.s^{-1}]
w	net consumed work [J]
x	horizontal space coordinate [m]
y	vertical space coordinate [m]

Greek letters

γ	interface function [−]
Γ_1, Γ_2, Γ_3, Γ_4, Γ_i	spatial boundary [−]
$\Delta\mathcal{C}$	relative improvement compared to the reference [−]
Δt	time step [s]
Δx, Δy	space mesh [m]
ΔX, ΔY	urban canyon size [m]
ε, ϵ	error [K]
θ, δ	mesh ratio at the interface [−]
λ	heat conductivity [W.m^{-1}.K^{-1}]
Σ	scheme model coefficients [−]
Ω_p	interface parameters domain [−]
Ω_t	time domain [−]
Ω, Ω_1, Ω_2	space domain [−]

Subscripts and superscript

dr	direct flux component
df	diffuse flux component
rf	reflective flux component
∞, j	boundary of the face j
$\star$	dimensionless value or optimized parameters

in turn demands body-fitted meshes aligned with internal boundaries. While effective, such strategies significantly increase meshing complexity and computational cost, particularly for time-dependent problems where interface positions may evolve.

To overcome these limitations, recent advances have introduced topological optimization frameworks that explicitly account for the spatial configuration of internal regions under heterogeneous boundary excitations [8–10]. These formulations typically aim to enhance global system performance, but many still rely on interpolated or homogenized representations across region boundaries, which can obscure sharp interfacial dynamics and localized phenomena [11].

To better resolve these effects, numerical methods capable of handling discontinuous domains with non-body-fitted meshes have been developed. The Ghost Fluid Method (GFM) [12,13] and the extended finite element method (XFEM) [14] are particularly notable in this context. These approaches capture jumps in fields and fluxes across internal interfaces while maintaining computational robustness on regular grids, making them suitable for problems involving irregular or evolving domain geometries.

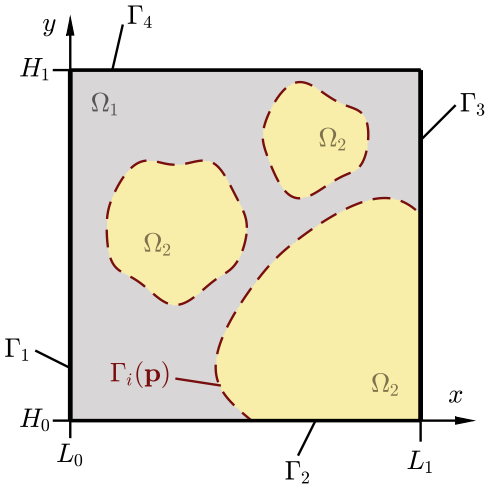

Fig. 1. Illustration of the mathematical model.

Alongside these advances in interface modeling, the development of efficient time integration schemes remains critical to overcome many numerical difficulties and for enabling more realistic two-dimensional simulations [15–17]. These include the Method of Horizontal Lines MOHL [1], adaptive spatio-temporal meshing methods [18], and explicit finite difference schemes such as the DuFort–Frankel method offer a compelling compromise between stability and computational cost. Originally developed for parabolic problems, this scheme avoids restrictive time step limitations associated with classical explicit methods, enabling stable and fast simulations without resorting to implicit solvers. Its combination with mesh-agnostic interface methods like GFM opens new perspectives for accurate and efficient simulation of complex transient diffusion problems in composite geometries.

This paper aims to introduce a novel and computationally efficient numerical model for transient diffusion in composite domains with discontinuous interface conditions between subdomains. The proposed approach is based on a finite difference formulation that combines the DuFort–Frankel scheme with the GFM, allowing for accurate resolution of discontinuities across internal boundaries while retaining a regular Cartesian grid. It enables the simulation of diffusive processes in multi-material domains with shaped interface, ensuring both field and flux continuity across interfaces with jump conditions. The formulation also accommodates complex boundary conditions, including radiative and convective effects, while maintaining a very low computational cost. The mathematical formulation of the problem is presented in Section 2, followed by a detailed description of the numerical model in Section 3. The model is then validated in Section 4 in several stages, including a benchmark comparison with an analytical solution, where its performance is assessed against established models from the literature, and a comparison with a finite element code. Finally, the remainder of the work is devoted to applying the proposed method to a case of energy improvement of the topology of building walls.

2. Mathematical model

The physical model considers a two-dimensional transient heat conduction problem. It is studied in coordinate space $\mathbf{x} = (x, y)$ in a domain Ω of height $H_1 - H_0$ [m] and width $L_1 - L_0$ [m], delimited by the boundaries $\Gamma = \bigcup_{j=1}^{4} \Gamma_j$, illustrated in Fig. 1, and in time domain $\Omega_t = [0, t_f]$.

2.1. Governing equations

The main domain Ω is a composite domain comprising two distinct sub-domains Ω_1 and Ω_2, separated by a non-planar interface Γ_i:

$$\Gamma_i(\mathbf{p}) = \left\{ \mathbf{x} \in \mathbb{R}^2 \mid \gamma(\mathbf{x}, \mathbf{p}) = 0,\ \mathbf{x} \in \Omega,\ \mathbf{p} \in \Omega_p \right\}$$

with $\gamma(\mathbf{x}, \mathbf{p})$ an implicit function governed by N_p parameters: $\mathbf{p} = \left(p_1, \ldots, p_{N_p}\right) \in \Omega_p$.

Each sub-domain has different, space-dependent thermal properties, λ [W.m^{-1}.K^{-1}] the thermal conductivity, c [J.m^{-3}.K^{-1}] the heat capacity by volume, and f [W.m^{-3}] the volumetric heat source term. If we assume λ_1, c_1 and f_1 the properties in Ω_1 and λ_2, c_2 and f_2 the properties in Ω_2, then the properties in Ω are defined by a Heaviside function $\mathcal{H}$.

$$\lambda(\mathbf{x}) = \lambda_1(\mathbf{x}) \cdot \left(1 - \mathcal{H}\left[\gamma(\mathbf{x}, \mathbf{p})\right]\right) + \lambda_2(\mathbf{x}) \cdot \mathcal{H}\left[\gamma(\mathbf{x}, \mathbf{p})\right], \qquad \forall \mathbf{x} \in \Omega$$

$$c(\mathbf{x}) = c_1(\mathbf{x}) \cdot \left(1 - \mathcal{H}\left[\gamma(\mathbf{x}, \mathbf{p})\right]\right) + c_2(\mathbf{x}) \cdot \mathcal{H}\left[\gamma(\mathbf{x}, \mathbf{p})\right], \qquad \forall \mathbf{x} \in \Omega$$

$$f(\mathbf{x}) = f_1(\mathbf{x}) \cdot \left(1 - \mathcal{H}\left[\gamma(\mathbf{x}, \mathbf{p})\right]\right) + f_2(\mathbf{x}) \cdot \mathcal{H}\left[\gamma(\mathbf{x}, \mathbf{p})\right], \quad \forall \mathbf{x} \in \Omega$$

Then, the governing heat transfer equation is:

$$\frac{\partial}{\partial x}\left(\lambda(\mathbf{x}) \frac{\partial T}{\partial x}\right) + \frac{\partial}{\partial y}\left(\lambda(\mathbf{x}) \frac{\partial T}{\partial y}\right) + f(\mathbf{x}, t) = c(\mathbf{x}) \frac{\partial T}{\partial t}, \quad \forall \mathbf{x} \in \Omega \tag{1}$$

At the initial time, the domain is assumed to be in a state that satisfies the boundary conditions. This compatibility ensures a physically consistent starting point for the transient simulation.

$$T = T_0(\mathbf{x}), \quad \forall \mathbf{x} \in \Omega, \ t = 0$$

2.2. Boundary conditions

The boundary conditions of the domain Ω are time and space dependent. Two types of conditions will be considered. On the one hand, DIRICHLET type conditions where at the boundary Γ_j:

$$T = T_{\infty,j}(\mathbf{x}, t), \quad \forall \mathbf{x} \in \Gamma_j, \quad \forall j \in \{1, \dots, 4\} \tag{2}$$

On the other hand, ROBIN type conditions, in order to ensure equality between the diffusive flux in the domain and the combination of convective and radiative fluxes outside the domain.

$$\lambda(\mathbf{x}) \frac{\partial T}{\partial \mathbf{n}_j} = h_{\infty,j}(\mathbf{x}, t) \cdot \left(T_{\infty,j}(\mathbf{x}, t) - T\right) + q_{\infty,j}(\mathbf{x}, t), \quad \forall \mathbf{x} \in \Gamma_j, \quad \forall j \in \{1, \dots, 4\} \tag{3}$$

with $\mathbf{n}_j$ being the unit outward normal of the considered boundary Γ_j. $T_{\infty,j}$ [K] is the external temperature, $h_{\infty,j}$ [W.m^{-2}.K^{-1}] is the convective surface coefficient and $q_{\infty,j}$ [W.m^{-2}] is the incident short-wave radiation flux. These values are dependent on time and space.

At the interface between two materials, the temperatures of each material and the conductive heat flux is continuous depending on a jump conditions:

$$T\Big|_{\mathbf{x}+\boldsymbol{\epsilon}} - T\Big|_{\mathbf{x}-\boldsymbol{\epsilon}} = a(\mathbf{x}, t), \quad \forall \mathbf{x} \in \Gamma_i \tag{4a}$$

$$\lambda(\mathbf{x}) \frac{\partial T}{\partial \mathbf{n}^+}\bigg|_{\mathbf{x}+\boldsymbol{\epsilon}} - \lambda(\mathbf{x}) \frac{\partial T}{\partial \mathbf{n}^-}\bigg|_{\mathbf{x}-\boldsymbol{\epsilon}} = b(\mathbf{x}, t), \quad \forall \mathbf{x} \in \Gamma_i \tag{4b}$$

with $\boldsymbol{\epsilon}$ tending to a zero vector, so that $\mathbf{x} + \boldsymbol{\epsilon}$ denoting the interface on the side of subdomain Ω_2, and $\mathbf{x} - \boldsymbol{\epsilon}$ on the side of Ω_1, and thus $\mathbf{n}^+$ and $\mathbf{n}^-$ the normals at the interface from one sub-domain to the other so that $\mathbf{n}^+ = -\mathbf{n}^-$. The temperature jump a_{Γ_i} and the flux jump b_{Γ_i} are time and space dependant.

2.3. Dimensionless formulation

In order to facilitate efficient numerical computations and improve the generality of the numerical solver, a dimensionless formulation of the problem is introduced. The temperature field is non-dimensionalized using the following transformation:

$$u := \frac{T - T_{\text{ref}}}{\delta T} \tag{5}$$

where T_{ref} and δT are characteristic temperatures. This change of variable is also applied to the initial temperature condition T_0 and to the external boundary temperature T_∞. The spatial and temporal coordinates are rescaled as:

$$t^\star := \frac{t}{t_{\text{f}}}, \qquad x^\star := \frac{x}{L_1 - L_0}, \qquad y^\star := \frac{y}{H_1 - H_0}.$$

This choice allows the computational domain to be mapped onto the unit square $\Omega^\star = [0, 1] \times [0, 1]$. Then, the material properties, the heat source term, and the jump values are similarly rescaled:

$$\lambda^\star := \frac{\lambda}{\lambda_0}, \qquad c^\star := \frac{c}{c_0}, \qquad f^\star := \frac{f}{f_0}, \qquad a^\star := a \cdot \delta T, \qquad b^\star := \frac{b \cdot \delta T}{\lambda_0 \cdot \Delta_{HL}}.$$

with λ_0, c_0 and f_0 being reference values for the thermal conductivity, the volumetric heat capacity, and the heat source, and Δ_{HL} the following expression:

$$\Delta_{HL} = \sqrt{\left(|\mathbf{n}^+ \cdot \mathbf{e}_x^T| \cdot (L_1 - L_0)\right)^2 + \left(|\mathbf{n}^+ \cdot \mathbf{e}_y^T| \cdot (H_1 - H_0)\right)^2}$$

Several dimensionless numbers emerge naturally from this formulation and characterize the heat transfer phenomena:
The FOURIER numbers, which describe the diffusion of heat in each spatial direction:

$$\text{Fo}_\text{x} := \frac{\lambda_0 \cdot t_{\text{f}}}{c_0 \cdot (L_1 - L_0)^2}, \qquad \text{Fo}_\text{y} := \frac{\lambda_0 \cdot t_{\text{f}}}{c_0 \cdot (H_1 - H_0)^2}$$

The BIOT numbers, which quantify the intensity of convective heat exchange at the domain boundaries:

$$\mathrm{Bi}_j := \frac{h_{\infty,j}\cdot(L_1-L_0)}{\lambda_0},\quad \forall j\in\{1,3\},\qquad \mathrm{Bi}_j := \frac{h_{\infty,j}\cdot(H_1-H_0)}{\lambda_0},\quad \forall j\in\{2,4\}$$

A source intensity number S, which we introduce. This term quantifies the relative influence of the volumetric heat source on the thermal capacity of the material:

$$\mathrm{S} := \frac{f_0\cdot t_\mathrm{f}}{c_0\cdot\delta T}$$

The external radiative fluxes is also rescaled as:

$$q^\star_{\infty,j} := \frac{q_{\infty,j}\cdot(L_1-L_0)}{\lambda_0\cdot\delta T},\quad \forall j\in\{1,3\},\qquad q^\star_{\infty,j} := \frac{q_{\infty,j}\cdot(H_1-H_0)}{\lambda_0\cdot\delta T},\quad \forall j\in\{2,4\}$$

Finally, the dimensionless diffusion Eq. (1) can be written as:

$$\mathrm{Fo}_\mathrm{x}\cdot\frac{\partial}{\partial x^\star}\left(\lambda^\star\frac{\partial u}{\partial x^\star}\right)+\mathrm{Fo}_\mathrm{y}\cdot\frac{\partial}{\partial y^\star}\left(\lambda^\star\frac{\partial u}{\partial y^\star}\right)+\mathrm{S}\cdot f^\star = c^\star\frac{\partial u}{\partial t^\star} \tag{6}$$

with the initial condition $u=u_0$, and the boundary conditions from Eqs. (2) and (3):

$$\text{DIRICHLET}:\quad u=u_{\infty,j},\qquad \forall\mathbf{x}^\star\in\Gamma^\star_j,\quad \forall j\in\{1,\dots,4\} \tag{7a}$$

$$\text{ROBIN}:\quad \lambda^\star\frac{\partial u}{\partial\mathbf{n}^\star_j}+\mathrm{Bi}_j\cdot u=\mathrm{Bi}_j\cdot u_{\infty,j}+q^\star_{\infty,j},\qquad \forall\mathbf{x}^\star\in\Gamma^\star_j,\quad \forall j\in\{1,\dots,4\} \tag{7b}$$

and finally at the interface:

$$u\Big|_{\mathbf{x}^\star+\boldsymbol{\epsilon}^\star}-u\Big|_{\mathbf{x}^\star-\boldsymbol{\epsilon}^\star}=a^\star \tag{8a}$$

$$\lambda^\star(\mathbf{x}^\star)\cdot\frac{\partial u}{\partial\mathbf{n}^{\star+}}\Big|_{\mathbf{x}^\star+\boldsymbol{\epsilon}^\star}-\lambda^\star(\mathbf{x}^\star)\cdot\frac{\partial u}{\partial\mathbf{n}^{\star-}}\Big|_{\mathbf{x}^\star-\boldsymbol{\epsilon}^\star}=b^\star \tag{8b}$$

3. Numerical method

To solve the transient diffusion problem described above, a finite difference method is employed for its simplicity and low computational cost in the context of global regular domains. In the following, for the sake of clarity, we will omit the * symbols that are specific to dimensionless formulation. The Eq. (6) can then be generalized and simplified as follows:

$$\frac{\partial}{\partial x}\left(\Lambda^x\cdot\frac{\partial u}{\partial x}\right)+\frac{\partial}{\partial y}\left(\Lambda^y\cdot\frac{\partial u}{\partial y}\right)+\mathrm{F}=c\,\frac{\partial u}{\partial t} \tag{9}$$

where $\Lambda^x := \mathrm{Fo}_\mathrm{x}\cdot\lambda$, $\Lambda^y := \mathrm{Fo}_\mathrm{y}\cdot\lambda$, and $\mathrm{F} := \mathrm{S}\cdot f$.

Thus, a uniform discretisation in time and space is considered, with steps Δt for time, Δx for x space and Δy for y space. The discrete values $u(\mathbf{x},t)$ are written as $u^n_{ji} := u(x_j,y_i,t^n)$ with $i=\{1,\dots,N_y\}$, $j=\{1,\dots,N_x\}$ and $n=\{1,\dots,N_t\}$.

For numerical integration, the DUFORT-FRANKEL scheme is used to build an efficient numerical model. In addition, it allows the problem to be expressed explicitly, so that no costly matrix inversion is required, as is the case with implicit approaches. Furthermore, as shown in [17], the scheme has an extended stability region, i.e. a relaxed Courant-Friedrichs-Lewy (CFL) restriction [19]. The purpose is to extend the application of this scheme and its properties to interface problems involving discontinuities in both field and flux.

3.1. Governing scheme

First, we write the numerical scheme in its simplest form. That is, as it is expressed within a subdomain. Thus, Eq. (9) is written in a discretized form with central finite differences in space and according to a forward EULER scheme in time:

$$\begin{aligned}&\frac{1}{\Delta x}\left[\Lambda^x_{j+\frac12 i}\left(\frac{u^n_{j+1i}-u^n_{ji}}{\Delta x}\right)-\Lambda^x_{j-\frac12 i}\left(\frac{u^n_{ji}-u^n_{j-1i}}{\Delta x}\right)\right]\\&+\frac{1}{\Delta y}\left[\Lambda^y_{ji+\frac12}\left(\frac{u^n_{ji+1}-u^n_{ji}}{\Delta y}\right)-\Lambda^y_{ji-\frac12}\left(\frac{u^n_{ji}-u^n_{ji-1}}{\Delta y}\right)\right]+\mathrm{F}^n_{ji}=c_{ji}\,\frac{u^{n+1}_{ji}-u^n_{ji}}{\Delta t}\end{aligned} \tag{10}$$

where the coefficients Λ^x and Λ^y, characterizing diffusion along the x and y directions respectively, are evaluated between adjacent nodes of the mesh. For example:

$$\Lambda^x_{j+\frac12 i}=\Lambda^x\left(x_j+\frac{\Delta x}{2},\,y_i\right),\qquad \Lambda^y_{ji+\frac12}=\Lambda^y\left(x_j,\,y_i+\frac{\Delta y}{2}\right).$$

Then, to obtain the DuFort-Frankel scheme, it suffices to replace each occurrence of u_{ji}^{n} with $1/2 \cdot \left(u_{ji}^{n+1} + u_{ji}^{n-1}\right)$, and F_{ji}^{n} with $1/2 \cdot \left(\mathrm{F}_{ji}^{n+1} + \mathrm{F}_{ji}^{n-1}\right)$. After simplification, this leads to the following expression:

$$\begin{aligned} u_{ji}^{n+1} = {} & \Sigma_{j-\frac{1}{2}i} \cdot u_{j-1i}^{n} + \Sigma_{j+\frac{1}{2}i} \cdot u_{j+1i}^{n} + \Sigma_{ji-\frac{1}{2}} \cdot u_{ji-1}^{n} \\ & + \Sigma_{ji+\frac{1}{2}} \cdot u_{ji+1}^{n} + \Sigma_{ji} \cdot u_{ji}^{n-1} + \frac{1}{2}\left(\Phi_{ji}^{n+1} + \Phi_{ji}^{n-1}\right) \end{aligned} \tag{11}$$

where the coefficients are given by:

$$\Sigma_{j-\frac{1}{2}i} := \frac{2\,k_{j-\frac{1}{2}i}}{1+\mathrm{K}}, \qquad \Sigma_{j+\frac{1}{2}i} := \frac{2\,k_{j+\frac{1}{2}i}}{1+\mathrm{K}}, \qquad \Sigma_{ji-\frac{1}{2}} := \frac{2\,k_{ji-\frac{1}{2}}}{1+\mathrm{K}},$$

$$\Sigma_{ji+\frac{1}{2}} := \frac{2\,k_{ji+\frac{1}{2}}}{1+\mathrm{K}}, \qquad \Sigma_{ji} := \frac{1-\mathrm{K}}{1+\mathrm{K}},$$

$$k_{j-\frac{1}{2}i} := \frac{\Delta t \cdot \Lambda^{x}_{\,j-\frac{1}{2}i}}{\Delta x^2 \cdot c_{ji}}, \qquad k_{j+\frac{1}{2}i} := \frac{\Delta t \cdot \Lambda^{x}_{\,j+\frac{1}{2}i}}{\Delta x^2 \cdot c_{ji}}, \qquad k_{ji-\frac{1}{2}} := \frac{\Delta t \cdot \Lambda^{y}_{\,ji-\frac{1}{2}}}{\Delta y^2 \cdot c_{ji}},$$

$$k_{ji+\frac{1}{2}} := \frac{\Delta t \cdot \Lambda^{y}_{\,ji+\frac{1}{2}}}{\Delta y^2 \cdot c_{ji}}, \qquad \mathrm{K} := k_{j-\frac{1}{2}i} + k_{j+\frac{1}{2}i} + k_{ji-\frac{1}{2}} + k_{ji+\frac{1}{2}}.$$

and the source terms coefficients by:

$$\Phi_{ji}^{n+1} = \frac{\mathrm{F}_{ji}^{n+1}}{c_{ji}\,(1+\mathrm{K})}, \qquad \Phi_{ji}^{n-1} = \frac{\mathrm{F}_{ji}^{n-1}}{c_{ji}\,(1+\mathrm{K})}.$$

Finally, Eq. (11) can be recast in a compact form by introducing the vector $\underline{\mathbf{u}}^{n} = [u_1^n, \ldots, u_k^n, \ldots, u_N^n]^{\mathrm{T}}$ representing the discrete solution at time step n, where the global index is given by $k = j + N_y \cdot (i-1)$, and $N = N_x \cdot N_y$ is the total number of spatial nodes. This leads to the following system:

$$\underline{\mathbf{u}}^{n+1} = \underline{\underline{\mathbf{A}}} \cdot \underline{\mathbf{u}}^{n} + \underline{\underline{\mathbf{B}}} \cdot \underline{\mathbf{u}}^{n-1} + \underline{\mathbf{\Phi}}^{n} \tag{12}$$

We note that matrix $\underline{\underline{\mathbf{A}}}$ is a sparse band matrix with non-zero entries on the first sub- and super-diagonals, as well as on the diagonals offset by $\pm N_y$, while the main diagonal remains zero. Similarly, matrix $\underline{\underline{\mathbf{B}}}$ is a diagonal matrix, with non-zero entries only along its main diagonal. In addition, the source terms at time steps $n+1$ and $n-1$ are combined into a single expression $\underline{\mathbf{\Phi}}^{n}$ to improve readability.

3.2. Interface handling between subdomains

The numerical integration at nodes located near the interface Γ_i is based on the Ghost Fluid Method (GFM), described in detail in [13]. In the present approach, the interface Eq. (8) are approximated by assuming that the normal vector to the interface $\mathbf{n}$ is aligned with the mesh axis it intersects, namely the x- or y-direction. This assumption simplifies the numerical computations by restricting the flux evaluation to directions aligned with the mesh axes.

To illustrate the modification of Eq. (11) at the interface between two materials, we consider the configuration depicted in Fig. 2. In this case, the interface Γ_i crosses between the nodes $\mathbf{x}_{j\,i}$ - $\mathbf{x}_{j+1\,i}$ and $\mathbf{x}_{j\,i}$ - $\mathbf{x}_{j\,i+1}$. The interface conditions given in Eq. (8) are first approximated separately along the x- and y-directions, involving ghost nodes located on either side of the interface: u_{j-} and u_{j+} along the x-axis, and u_{i-} and u_{i+} along the y-axis. Along the x-axis the discretization of Eq. (8) leads to:

$$u_{j+}^{n} - u_{j-}^{n} = a_j^n, \qquad \lambda_{j+1i} \cdot \frac{u_{j+1i}^{n} - u_{j+}^{n}}{(1-\theta)\,\Delta x} - \lambda_{ji} \cdot \frac{u_{j-}^{n} - u_{ji}^{n}}{\theta\,\Delta x} = b_j^n \tag{13}$$

and along the y-axis:

$$u_{i+}^{n} - u_{i-}^{n} = a_i^n, \qquad \lambda_{ji+1} \cdot \frac{u_{ji+1}^{n} - u_{i+}^{n}}{(1-\delta)\,\Delta y} - \lambda_{ji} \cdot \frac{u_{i-}^{n} - u_{ji}^{n}}{\delta\,\Delta y} = b_i^n \tag{14}$$

with:

$$a_j^n := a\big(x_i + \theta\,\Delta x,\, y_j,\, t^n\big), \qquad a_i^n := a\big(x_i,\, y_j + \delta\,\Delta y,\, t^n\big),$$

$$b_j^n := b\big(x_i + \theta\,\Delta x,\, y_j,\, t^n\big), \qquad b_i^n := b\big(x_i,\, y_j + \delta\,\Delta y,\, t^n\big).$$

Here θ and δ are respectively the ratio of the distance along the x-axis and the y-axis between the $\mathbf{x}_{j\,i}$ node and the interface. The expressions of θ and δ depends on the interface parametric function. For example, if γ represents the distance along x from the interface, then θ will take the following form: $\theta = |\gamma_{ji}| \,/\, \left(|\gamma_{j+1i}| + |\gamma_{ji}|\right)$ and $\delta = |\gamma_{ji}^{-1}| \,/\, \left(|\gamma_{ji+1}^{-1}| + |\gamma_{ji}^{-1}|\right)$.

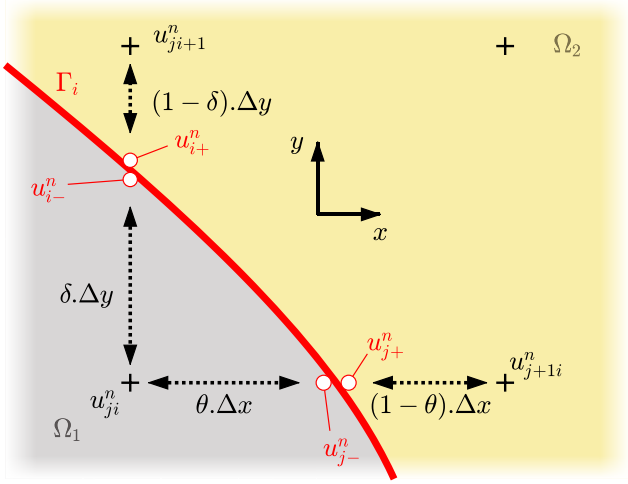

Fig. 2. Illustration of the simplified Ghost Fluid Method.

Subsequently, at node $\mathbf{x}_{j\,i}$, the previously discretized Eq. (10) is adapted to the presence of the interface by introducing the ghost nodes.

$$\begin{aligned}&\frac{1}{\Delta x}\left[\Lambda^x_{ji}\left(\frac{u^n_{j-}-u^n_{ji}}{\theta\,\Delta x}\right)-\Lambda^x_{j-\frac{1}{2}i}\left(\frac{u^n_{ji}-u^n_{j-1i}}{\Delta x}\right)\right]\\&+\frac{1}{\Delta y}\left[\Lambda^y_{ji}\left(\frac{u^n_{i-}-u^n_{ji}}{\delta\,\Delta y}\right)-\Lambda^y_{ji-\frac{1}{2}}\left(\frac{u^n_{ji}-u^n_{ji-1}}{\Delta y}\right)\right]+\mathrm{F}^n_{ji}=c_{ji}\,\frac{u^{n+1}_{ji}-u^n_{ji}}{\Delta t}\end{aligned}\tag{15}$$

Then, by isolating the derivatives with ghost terms using the previously derived expressions (13) and (14), it gives:

$$\begin{aligned}\frac{u^n_{j-}-u^n_{ji}}{\theta\,\Delta x}&=\frac{\widehat{\lambda}_x}{\lambda_{ji}}\cdot\frac{u^n_{j+1i}-a^n_i-u^n_{ji}}{\Delta x}+\frac{\widehat{\lambda}_x}{\lambda_{ji}}\cdot\frac{b^n_i\,(1-\theta)}{\lambda_{j+1i}}\\\frac{u^n_{i-}-u^n_{ji}}{\delta\,\Delta y}&=\frac{\widehat{\lambda}_y}{\lambda_{ji}}\cdot\frac{u^n_{ji+1}-a^n_j-u^n_{ji}}{\Delta y}+\frac{\widehat{\lambda}_y}{\lambda_{ji}}\cdot\frac{b^n_j\,(1-\delta)}{\lambda_{ji+1}}\end{aligned}$$

with: $\widehat{\lambda}_x=\frac{\lambda_{ji}\cdot\lambda_{j+1i}}{\lambda_{j+1i}\cdot\theta+\lambda_{ji}\cdot(1-\theta)}$, $\widehat{\lambda}_y=\frac{\lambda_{ji}\cdot\lambda_{ji+1}}{\lambda_{ji+1}\cdot\delta+\lambda_{ji}\cdot(1-\delta)}$. and substituting them into Eq. (15), to which the DuFort–Frankel scheme is applied, one obtains an expression similar in form to Eq. (11). This new expression includes additional and modified terms arising from the jump conditions:

$$\begin{aligned}u^{n+1}_{ji}=&\,\Sigma_{j-\frac{1}{2}i}\cdot u^n_{j-1i}+\Sigma_{j+\frac{1}{2}i}\cdot u^n_{j+1i}+\Sigma_{ji-\frac{1}{2}}\cdot u^n_{ji-1}+\Sigma_{ji+\frac{1}{2}}\cdot u^n_{ji+1}+\Sigma_{ji}\cdot u^{n-1}_{ji}\\&+\frac{1}{2}\left(\Phi^{n+1}_{ji}+\Phi^{n-1}_{ji}\right)+\frac{1}{2}\left(\widetilde{a}^{n+1}_j+\widetilde{a}^{n-1}_j\right)+\frac{1}{2}\left(\widetilde{a}^{n+1}_i+\widetilde{a}^{n-1}_i\right)\\&+\frac{1}{2}\left(\widetilde{b}^{n+1}_j+\widetilde{b}^{n-1}_j\right)+\frac{1}{2}\left(\widetilde{b}^{n+1}_i+\widetilde{b}^{n-1}_i\right)\end{aligned}\tag{16}$$

with:

$$\begin{aligned}\widetilde{a}_j&=-\Sigma_{j+\frac{1}{2}i}\cdot a_j,\qquad\widetilde{b}_j=-\Sigma_{j+\frac{1}{2}i}\cdot\frac{(1-\theta)\,\Delta x}{\lambda_{j+1i}}\,b_j,\\\widetilde{a}_i&=-\Sigma_{ji+\frac{1}{2}}\cdot a_i,\qquad\widetilde{b}_i=-\Sigma_{ji+\frac{1}{2}}\cdot\frac{(1-\delta)\,\Delta y}{\lambda_{ji+1}}\,b_i,\end{aligned}$$

where coefficients $\Sigma_{j-\frac{1}{2}i}$, $\Sigma_{j+\frac{1}{2}i}$, $\Sigma_{ji-\frac{1}{2}}$, $\Sigma_{ji+\frac{1}{2}}$ and Σ_{ji}, defined in Eq. (11), are modified due to:

$$k_{j+\frac{1}{2}i}=\frac{\Delta t\cdot\Lambda^x_{ji}}{\Delta x^2\cdot c_{ji}}\cdot\frac{\widehat{\lambda}_x}{\lambda_{ji}},\qquad k_{ji+\frac{1}{2}}=\frac{\Delta t\cdot\Lambda^y_{ji+\frac{1}{2}}}{\Delta y^2\cdot c_{ji}}\cdot\frac{\widehat{\lambda}_y}{\lambda_{ji}}.$$

The modified terms vary depending on the node under consideration. For instance, in the configuration shown in Fig. 2, if node $\mathbf{x}_{j+1\,i}$ is taken as the current node, only the interface aligned with the x-axis is considered. Consequently, Eq. (15) is modified as follows:

$$\begin{aligned}&\frac{1}{\Delta x}\left[\Lambda^x_{ji}\left(\frac{u^n_{j+1i}-u^n_{ji}}{\Delta x}\right)-\Lambda^x_{j-\frac{1}{2}i}\left(\frac{u^n_{ji}-u^n_{j+}}{(1-\theta)\,\Delta x}\right)\right]\\&+\frac{1}{\Delta y}\left[\Lambda^y_{ji}\left(\frac{u^n_{ji+1}-u^n_{ji}}{\Delta y}\right)-\Lambda^y_{ji-\frac{1}{2}}\left(\frac{u^n_{ji}-u^n_{ji-1}}{\Delta y}\right)\right]+\mathrm{F}^n_{ji}=c_{ji}\,\frac{u^{n+1}_{ji}-u^n_{ji}}{\Delta t}\end{aligned} \tag{17}$$

which, after simplification, becomes:

$$\begin{aligned}u^{n+1}_{ji}=&\,\Sigma_{j-\frac{1}{2}i}\cdot u^n_{j-1i}+\Sigma_{j+\frac{1}{2}i}\cdot u^n_{j+1i}+\Sigma_{ji-\frac{1}{2}}\cdot u^n_{ji-1}+\Sigma_{ji+\frac{1}{2}}\cdot u^n_{ji+1}+\Sigma_{ji}\cdot u^{n-1}_{ji}\\&+\frac{1}{2}\left(\Phi^{n+1}_{ji}+\Phi^{n-1}_{ji}\right)+\frac{1}{2}\left(\widetilde{a}^{n+1}_j+\widetilde{a}^{n-1}_j\right)+\frac{1}{2}\left(\widetilde{b}^{n+1}_j+\widetilde{b}^{n-1}_j\right)\end{aligned} \tag{18}$$

with:

$$\widetilde{a}_j=\Sigma_{j-\frac{1}{2}i}\cdot a_j,\qquad \widetilde{b}_j=-\Sigma_{j-\frac{1}{2}i}\cdot\frac{\theta\,\Delta x}{\lambda_{j-1i}}\,b_j,\qquad k_{j-\frac{1}{2}i}=\frac{\Delta t\cdot\Lambda^x_{ji}}{\Delta x^2\cdot c_{ji}}\cdot\frac{\widehat{\lambda}_x}{\lambda_{ji}}.$$

It can be observed that the jump coefficients in the y-direction are absent, since no interface intersects the node pairs $\mathbf{x}_{j+1\,i}$ - $\mathbf{x}_{j+1\,i+1}$, and $\mathbf{x}_{j+1\,i}$ - $\mathbf{x}_{j+1\,i-1}$ shown in Fig. 2.

Accordingly, the modified compact formulation Eq. (12) can be written as:

$$\underline{\mathbf{u}}^{n+1}=\underline{\underline{\mathbf{A}}}\cdot\underline{\mathbf{u}}^n+\underline{\underline{\mathbf{B}}}\cdot\underline{\mathbf{u}}^{n-1}+\underline{\mathbf{\Phi}}^n+\underline{\widetilde{\mathbf{a}}}^n+\underline{\widetilde{\mathbf{b}}}^n \tag{19}$$

Note that the structure of the matrix filling for $\underline{\underline{\mathbf{A}}}$ and $\underline{\underline{\mathbf{B}}}$ remains unchanged, since the same nodal values of $\underline{\mathbf{u}}$ are involved. Furthermore, the jump terms at time steps $n+1$ and $n-1$ have been grouped into two vectors $\underline{\widetilde{\mathbf{a}}}^n$ and $\underline{\widetilde{\mathbf{b}}}^n$ for clarity.

3.3. Treatment of boundary conditions

Without loss of generality, only the case of ROBIN conditions for a face and a corner of the main domain will be presented. Consider the Γ_1 surface where $x=L_0$. Eq. (7b), discretized to second order and at time step $n+1$, is written as follow:

$$\frac{\lambda_{1i}}{\Delta x}\left(-\frac{3}{2}\,u^{n+1}_{1i}+2\,u^{n+1}_{2i}-\frac{1}{2}\,u^{n+1}_{3i}\right)=\mathrm{Bi}^{n+1}_{1i,\,1}\cdot\left(u^{n+1}_{1i}-u^{n+1}_{\infty i,\,1}\right)-q^{n+1}_{\infty i,\,1}$$

Then the terms u^{n+1}_{2i} and u^{n+1}_{3i} are replaced using their expression in Eq. (11):

$$\begin{aligned}u^{n+1}_{1i}=&\,2\,\mathrm{a}_1\left(\Sigma_{\frac{3}{2}i}\cdot u^n_{1i}+\Sigma_{\frac{5}{2}i}\cdot u^n_{3i}+\Sigma_{2\,i-\frac{1}{2}}\cdot u^n_{2i-1}+\Sigma_{2\,i+\frac{1}{2}}\cdot u^n_{2i+1}+\Sigma_{2i}\cdot u^{n-1}_{2i}\right)\\&+\frac{\mathrm{a}_1}{2}\left(\Sigma_{\frac{5}{2}i}\cdot u^n_{2i}+\Sigma_{\frac{7}{2}i}\cdot u^n_{4i}+\Sigma_{3\,i-\frac{1}{2}}\cdot u^n_{3i-1}+\Sigma_{3\,i+\frac{1}{2}}\cdot u^n_{3i+1}+\Sigma_{3i}\cdot u^{n-1}_{3i}\right)\\&+\mathrm{a}_1\left(\Phi^{n+1}_{2i}+\Phi^{n-1}_{2i}+\frac{1}{4}\Phi^{n+1}_{3i}+\frac{1}{4}\Phi^{n-1}_{3i}\right)+\mathrm{b}_1\cdot u^{n+1}_{\infty i,1}+\mathrm{c}_1\cdot q^{n+1}_{\infty i,1}\end{aligned} \tag{20}$$

with η_1, μ_1 and ν_1 denoting the following coefficients, hereafter written without subscripts, but varying in both time and space:

$$\eta_1:=\frac{\lambda_{1i}\cdot\nu_1}{\Delta x},\qquad \mu_1:=\mathrm{Bi}^{n+1}_{1i,\,1}\cdot\nu_1,\qquad \nu_1:=\left(\mathrm{Bi}^{n+1}_{1i,\,1}+\frac{3}{2}\cdot\frac{\lambda_{1i}}{\Delta x}\right)^{-1}.$$

To treat the corners, we consider the specific case of the lower-left corner at $x=L_0$ and $y=H_0$. We begin by formulating the boundary conditions as if dealing with a surface perpendicular to the x-axis.

$$u^{n+1}_{11}=2\,\eta_1\cdot u^{n+1}_{21}+\frac{\eta_1}{2}\cdot u^{n+1}_{31}+\mu_1\cdot u^{n+1}_{\infty i,\,1}+\nu_1\cdot q^{n+1}_{\infty i,\,1} \tag{21}$$

The same approach is then applied to u^{n+1}_{21} and u^{n+1}_{31}, located on Γ_2 perpendicular to the y-axis:

$$\begin{aligned}u^{n+1}_{21}&=2\,\eta_2\cdot u^{n+1}_{22}+\frac{\eta_1}{2}\cdot u^{n+1}_{23}+\mu_2\cdot u^{n+1}_{\infty i,\,2}+\nu_2\cdot q^{n+1}_{\infty i,\,2}\\u^{n+1}_{31}&=2\,\eta_2\cdot u^{n+1}_{32}+\frac{\eta_1}{2}\cdot u^{n+1}_{33}+\mu_2\cdot u^{n+1}_{\infty i,\,2}+\nu_2\cdot q^{n+1}_{\infty i,\,2}\end{aligned}$$

Thus, u^{n+1}_{11} is obtained by expressing explicitly u^{n+1}_{21} and u^{n+1}_{31} as in Eq. (20), and substituting them into Eq. (21).

Finally, as previously, the boundary conditions can be written in a compact form that groups together all the boundary conditions treated in a similar way to the face and corner detailed above. $\underline{\underline{\mathbf{A_b}}}^{n+1}$ and $\underline{\underline{\mathbf{B_b}}}^{n+1}$ are sparse matrices with a partially banded structure: for the faces, $\underline{\underline{\mathbf{A_b}}}^{n+1}$ has 8 bands and $\underline{\underline{\mathbf{B_b}}}^{n+1}$ has 2; for the corners, $\underline{\underline{\mathbf{A_b}}}^{n+1}$ has 12 bands and $\underline{\underline{\mathbf{B_b}}}^{n+1}$ has 4.

$$\underline{\mathbf{u}}^{n+1}=\underline{\underline{\mathbf{A_b}}}^{n+1}\cdot\underline{\mathbf{u}}^n+\underline{\underline{\mathbf{B_b}}}^{n+1}\cdot\underline{\mathbf{u}}^{n-1}+\underline{\mathbf{\Phi_b}}+\left(\underline{\mathbf{C}}^{n+1}\right)^T\cdot\underline{\mathbf{u}_\infty}^{n+1}+\left(\underline{\mathbf{D}}^{n+1}\right)^T\cdot\underline{\mathbf{q}_\infty}^{n+1} \tag{22}$$

Table 1
Thermal properties of the material composing the domain.

Domain	*Material*	*Thermal conductivity* [W.m^{-1}.K^{-1}]	*Volumetric heat capacity* [MJ.m^{-3}.K^{-1}]
Ω_1	concrete	2	1.94
Ω_2	insulation	0.04	0.026

Table 2
Surface convective coefficient values.

Coefficients	h_{10} [W.m^{-2}.K^{-1}]	h_{11} [W.m^{-2}.K^{-1}]	h_{20} [W.m^{-2}.K^{-1}]	h_{21} [W.m^{-2}.K^{-1}]
Values	5.82	3.96	0.1	3

3.4. Global formulation

To conclude, the numerical model over the entire domain Ω is constructed by combining Eqs. (19) and (22):

$$\begin{aligned}\underline{\mathbf{u}}^{n+1} = &\left(\underline{\underline{\mathbf{A}}} + \underline{\underline{\mathbf{A}_\mathbf{b}}}^{n+1}\right) \cdot \underline{\mathbf{u}}^{n} + \left(\underline{\underline{\mathbf{B}}} + \underline{\underline{\mathbf{B}_\mathbf{b}}}^{n+1}\right) \cdot \underline{\mathbf{u}}^{n-1} + \underline{\mathbf{\Phi}}^{n} + \underline{\mathbf{\Phi}_\mathbf{b}}^{n} \\ &+ \underline{\widetilde{\mathbf{a}}}^{n} + \underline{\widetilde{\mathbf{b}}}^{n} + \left(\underline{\mathbf{C}}^{n+1}\right)^{T} \cdot \underline{\mathbf{u}_\infty}^{n+1} + \left(\underline{\mathbf{D}}^{n+1}\right)^{T} \cdot \underline{\mathbf{q}_\infty}^{n+1}\end{aligned} \tag{23}$$

The sparse matrix structure is carefully designed to ensure computational efficiency. In particular, the time-independent matrices $\underline{\underline{\mathbf{A}}}$ and $\underline{\underline{\mathbf{B}}}$ are assembled once at the beginning of the simulation. In contrast, the sparse matrices $\underline{\underline{\mathbf{A}_\mathbf{b}}}$ and $\underline{\underline{\mathbf{B}_\mathbf{b}}}$, which encode the boundary conditions, as well as all time-dependent sparse vectors, are initialized at the start and subsequently updated at each time step.

4. Verification of the model

To validate the implementation and assess the theoretical properties of the model, numerical results are compared both to an analytical solution and to those obtained with a final element solver. This dual comparison enables the evaluation of all key features of the model. The analytical solution [20] corresponds to a configuration with DIRICHLET boundary conditions, interface jump conditions, and a non-zero source term, all varying in both time and space. The final element solver, on the other hand, is applied to a scenario representative of realistic applications, with time and space dependent ROBIN boundary conditions, but no jumps and source terms. The finite element results are obtained using the `Partial Differential Equation Toolbox` of `Matlab` [21].

The accuracy of the model is assessed by computing both the L^2 and L^∞ norms of the error. For the comparison with the analytical solution, the error is directly evaluated on the finite difference model grid. In contrast, for the comparison with the finite element solver, the results are first interpolated onto the finite difference grid using the `interpolateSolution` function [22], before computing the errors. The L^2 error is defined as

$$\epsilon_2 = \left(\frac{1}{N}\sum_{j,i,n}\left(u_{\text{ref}}(x_j, y_i, t^n) - u(x_j, y_i, t^n)\right)^2\right)^{1/2} \tag{24}$$

where N is the total number of spatio-temporal points. A variant of this norm, denoted ϵ_2, is also employed, particularly to visualize the spatial distribution of the errors:

$$\epsilon_2(\mathbf{x}) = \left(\frac{1}{N_t}\sum_{n}\left(u_{\text{ref}}(\mathbf{x}, t^n) - u(\mathbf{x}, t^n)\right)^2\right)^{1/2}$$

The L^∞ error is computed as:

$$\epsilon_\infty = \max_{j,i,n}\left|u_{\text{ref}}(x_j, y_i, t^n) - u(x_j, y_i, t^n)\right| \tag{25}$$

Here, u_{ref} denote the reference solution, evaluated at each node and time step.

For all validation cases, the dimensionless quantities defined in Section 2.3 are computed using the physical thermal properties listed in the Table 1 and the convective coefficients Table 2 detailed in Section 4.2.

4.1. Analytical validation

The analytical reference solution, presented in detail in [20], is defined over the spatial domain $\Omega = [-1, 1] \times [-1, 1]$ and the temporal domain $\Omega_t = [0, 1]$. The interface Γ_i is represented by the following equation:

$$\gamma(\mathbf{x}, \mathbf{p}) = 0.5 + p_0 \cdot \sin\left(p_1 \cdot \arctan(y, x)\right) - \sqrt{x^2 + y^2}, \qquad \forall \mathbf{x} \in \Gamma_i$$

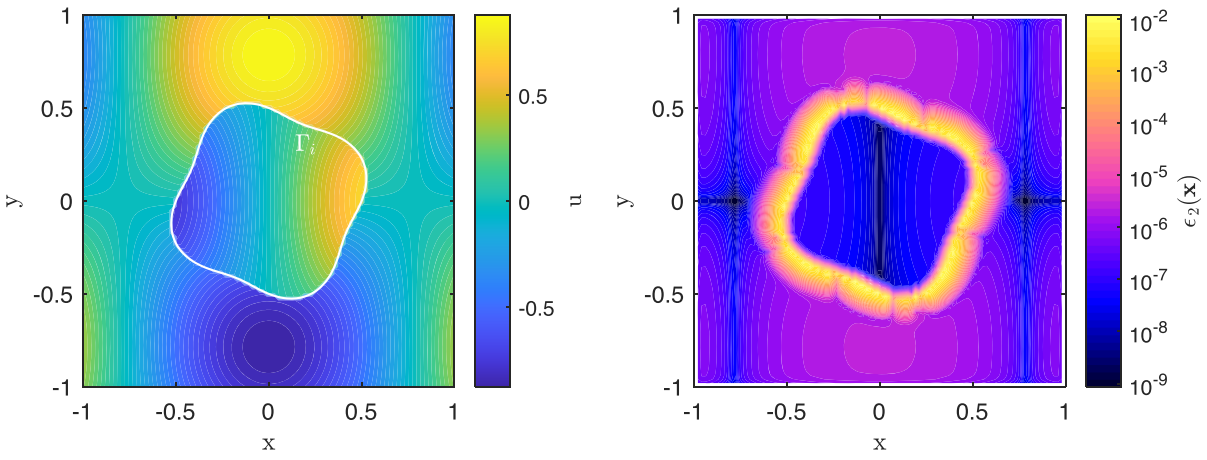

Fig. 3. Solution (a) and L^2 error fields (b) for case $\mathbf{p} = (0.05, 4)$.

The analytical solution is given by:

$$u(\mathbf{x}, t) = \cos(2\,x)\,\sin(2\,y)\,\cos(t), \qquad \forall\,\mathbf{x} \in \Omega_1$$
$$u(\mathbf{x}, t) = \sin(2\,x)\,\cos(2\,y)\,\cos(t), \qquad \forall\,\mathbf{x} \in \Omega_2$$

From this, the jump conditions across the interface are obtained analytically as:

$$[\,u\,]_\Gamma = \cos(t)\left(\cos(2\,x)\,\sin(2\,y) - \sin(2\,x)\,\cos(2\,y)\right)$$
$$\left[\,\lambda\,\frac{\partial u}{\partial \mathbf{n}}\,\right]_\Gamma = 2\cos(t)\Big(\sin(2\,x)\,\sin(2\,y)\cdot\left[\lambda_-\,\sin(\arctan(y,x)) - \lambda_+\,\cos(\arctan(y,x))\right] + \cos(2\,x)\,\cos(2\,y)\cdot\left[\lambda_+\,\sin(\arctan(y,x)) - \lambda_-\,\cos(\arctan(y,x))\right]\Big)$$

Substituting the analytical solution into the dimensionless formulation Eq. (6) yields the corresponding source term:

$$f(\mathbf{x}, t) = \left(4\,\lambda(\mathbf{x})\cdot\left(\mathrm{Fo_x} + \mathrm{Fo_y}\right)\,\cos(t) - c(\mathbf{x})\,\sin(t)\right)\,\cos(2\,x)\,\sin(2\,y), \qquad \forall\,\mathbf{x} \in \Omega_1$$
$$f(\mathbf{x}, t) = \left(4\,\lambda(\mathbf{x})\cdot\left(\mathrm{Fo_x} + \mathrm{Fo_y}\right)\,\cos(t) - c(\mathbf{x})\,\sin(t)\right)\,\sin(2\,x)\,\cos(2\,y), \qquad \forall\,\mathbf{x} \in \Omega_2$$

The initial and boundary conditions are directly derived from the analytical solution, evaluated at the spatial and temporal boundaries of the domain. The dimensionless coefficients are computed based on the physical thermal properties provided in Table 1.

First, the interface is constructed by selecting the values $\mathbf{p} = (p_0, p_1) = (0.05, 4)$ resulting in a regular squircle shape, as shown in Fig. 3(a), where the field distribution at the initial time is displayed. Fig. 3(b) presents the resulting error field for a mesh with $N_x = N_y = 100$ nodes and a time step $\Delta t = 10^{-3}$. It is observed that the maximum errors are concentrated near the interface and spread into the subdomain surrounding the squircle. This is because the strongest model approximations occur at the interface, where discontinuities and steep gradients are present as shown in Fig. 4. Indeed, the horizontal and vertical flux computed in the horizontal cross-section for Fig. 4(a) and (c), and the vertical cross-section for Fig. 4(b) and (d), neglect the normal vector at the interface. It may induce numerical artifacts analogous to the overheating phenomenon described in multimaterial flows [23]. Within the GFM, such omission can generate local entropy errors, producing flux overshoots or undershoots near interfaces despite accurate predictions of the primary field variables, *i.e.* the temperature in our case. The use of the interface nodes defined by the GFM to approximate the interface heat flux may lead to numerical artifacts. This behavior is conceptually rooted in earlier works [24,25], who showed that overheating arises when interfacial fluxes are applied without properly constraining the remaining degrees of freedom, leading to local overshoots in thermodynamic variables.

The errors Fig. 3(a) then propagate further into the subdomain characterized by the highest FOURIER values governing the diffusion process. Within each subdomain, the error is correlated with the magnitudes of the field values and fluxes, as illustrated in Figs. 3(a) and 4.

In a second step, we investigate the impact of the spatial steps on the model. To this end, the time step is fixed at $\Delta t = 10^{-4}$, and the number of nodes N_x and N_y are varied simultaneously between 8 and 500. The results obtained in Fig. 5, denoted DF for the DUFORT-FRANKEL scheme, are compared with those presented in [20] and extracted using a curve digitizing tool, where IM refers to an implicit EULER scheme with GFM integration, and ADI refers to the Alternating Direction Implicit method combined with the GFM. Focusing on the DF method, it can be observed that the model exhibits first-order accuracy for spatial steps between 10^{-2} and $3 \cdot 10^{-2}$ and second-order accuracy beyond this range. Since the DUFORT-FRANKEL scheme is theoretically second-order accurate in space [17], this suggests that the integration of the interface equations preserves, at least partially, the theoretical properties of the scheme.

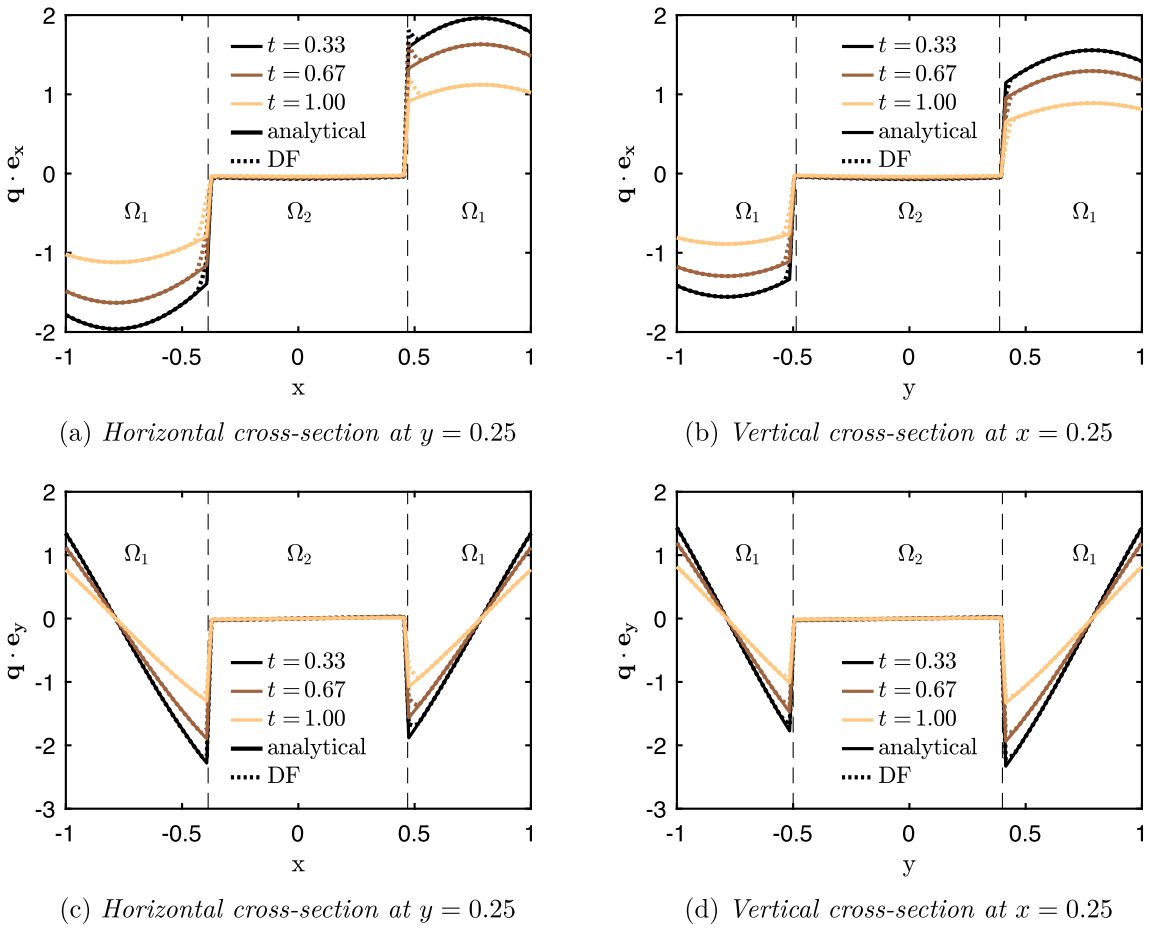

(a) *Horizontal cross-section at* $y = 0.25$ (b) *Vertical cross-section at* $x = 0.25$

(c) *Horizontal cross-section at* $y = 0.25$ (d) *Vertical cross-section at* $x = 0.25$

Fig. 4. Horizontal flux $\mathbf{q} \cdot \mathbf{e}_x$ and vertical flux $\mathbf{q} \cdot \mathbf{e}_y$ along two cross-sections (a-c) and dummyTXdummy– (b-d).

When comparing DF with the IM and ADI methods, it is observed that the L^2 norm exhibits very similar trends and magnitudes across the three approaches, whereas the L^∞ norm is slightly larger for DF. Given that ε_∞ is primarily influenced by errors at the interface, this discrepancy may be attributed to differences in the dimensionless coefficients, whose values are not specified in [20].

Lastly, the influence of the time discretization is also investigated by varying the time step Δt from 10^{-4} to 1 Fig. 6. This study is conducted for an interface defined by $\mathbf{p} = (0.25, 4)$, resulting in a two-headed curvature shape, and for the purpose of comparison with the results reported in [20]. Several theoretical results are confirmed through this analysis. First, the DF scheme is shown to be unconditionally stable, as expected. Moreover, the scheme initially exhibits second-order accuracy in time, before transitioning to first-order accuracy around $\Delta t = 10^{-1}$, when the accuracy condition is no longer satisfied [17]. Ultimately, the results can be compared with those obtained using the ADI method extracted from [20]. It can be observed that the error magnitudes are quite comparable, highlighting the effectiveness of the proposed DF scheme compared to an implicit method.

Finally, the numerical efficiency of the model was recorded for the following parameters: $N_x = N_y = 100$ and $\Delta t = 10^{-4}$. An average time of 6.6 seconds was obtained over multiple runs, which can be compared to the 201 seconds reported in [20] for the IM method using the same set of parameters. This highlights the efficiency of the proposed model. However, it should be noted that the software configuration used in [20] is not specified, whereas the computations of the developed model were performed on a system equipped with a Intel® Core™ `i7-14700F` CPU clocked at 5.3 GHz. The computational environment is based on the `Fortran` language, using the Intel® oneAPI HPC Toolkit [26] (version 2025.0), which enables parallelization of matrix computations.

4.2. Comparison with FEM

The second validation is conducted on a case similar to the realistic configuration studied in the final Section 5. It corresponds to the physical domain depicted in Fig. 9, where the interface is defined by a third-order polynomial function:

$$\gamma(\mathbf{x}, \mathbf{p}) = x - \left[d_1 + p_0 \frac{y}{H} \left(\frac{y}{H} - p_1 \right) \left(\frac{y}{H} - 1 \right) \right], \qquad \forall \mathbf{x} \in \Gamma_i \tag{26}$$

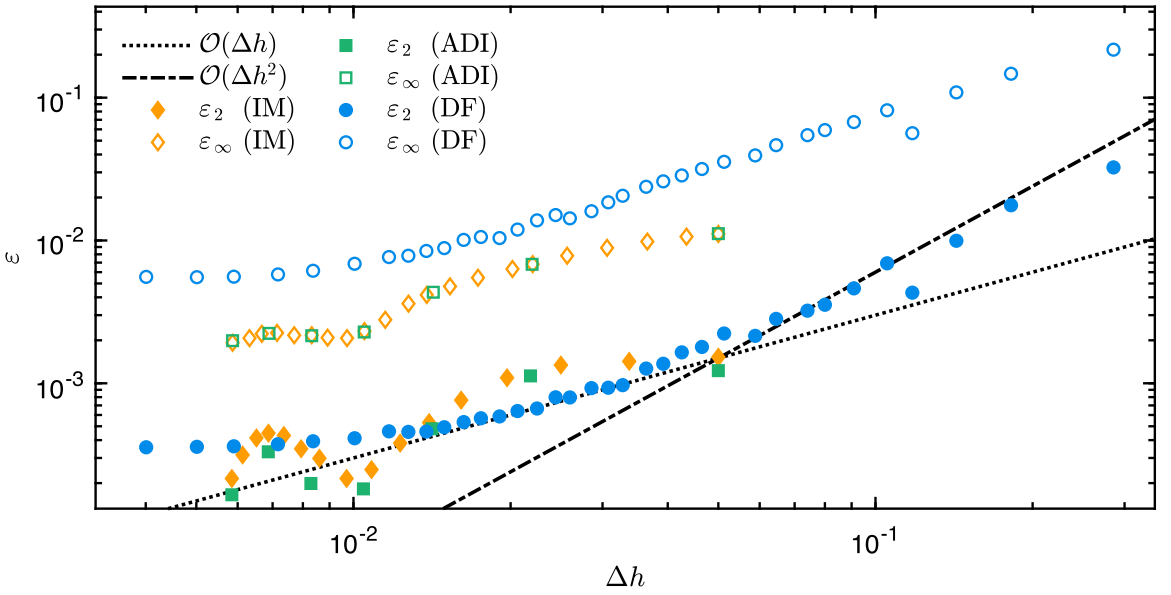

Fig. 5. Variation of the numerical models errors arccording to the spatial steps ($\Delta h = \Delta x = \Delta y$).

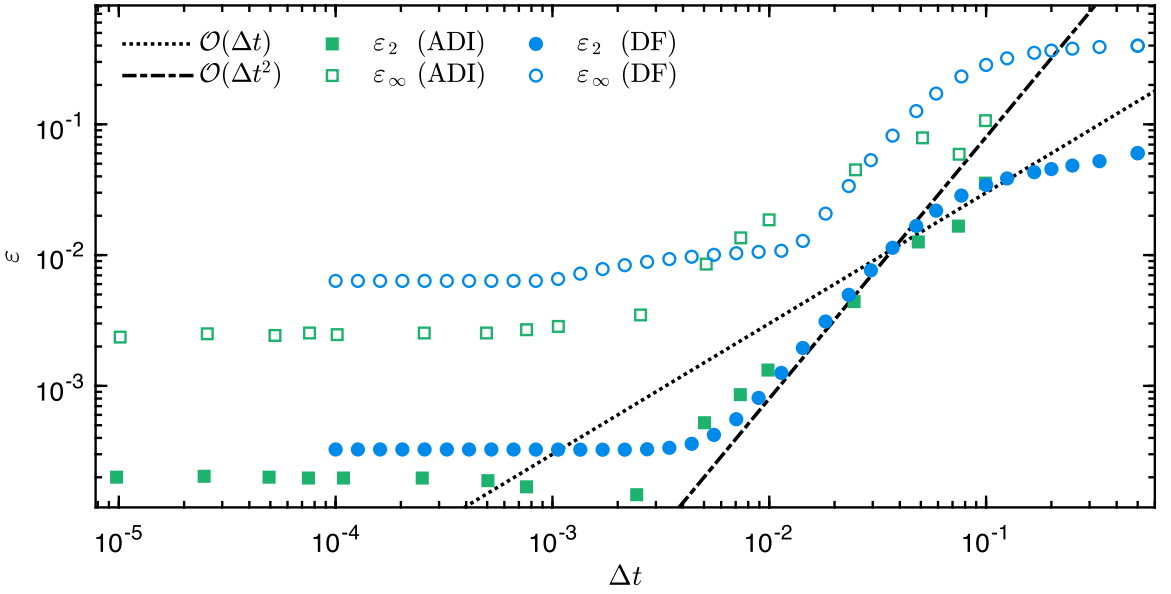

Fig. 6. Variation of the numerical models errors arccording to the time discretisation.

with $H = H_1 - H_0$, and d_1 the upper and lower anchoring points set at 0.2 m. Here, the parameters of the function are set to $\mathbf{p} = (p_0, p_1) = (1, 0.5)$. At the interface, temperature equality and continuity of the conductive flux are imposed, corresponding to zero jump conditions. Additionally, there are no source terms, and ROBIN boundary conditions are applied on Γ_1 and Γ_3, and NEUMANN boundary conditions on Γ_2 and Γ_4.

For boundary Γ_1, a time sinusoidal variation of temperature and heat flux are applied:

$$T_{\infty,1}(t) = T_{10}\,\cos(\omega_t \cdot t) + T_{11},$$
$$q_{\infty,1}(y,t) = q_{10}\left(1 + \tanh\left(q_{11} \cdot \left(y - \frac{H}{2}\right)\right)\right) \cdot \left|\sin(2\,\omega_t \cdot t + \psi)\right|.$$

with ω_t the angular frequency corresponding to a period of one day, ψ a time shift corresponding to 6 h, and the values $T_{10} = 5$ K, $T_{11} = 10$ °C, $q_{10} = 100$ W.m^{-2}.K^{-1} and $q_{11} = 10$. It is worth noting that the heat flux also exhibits a spatial variation, modeled by a

hyperbolic tangent profile, such that the flux is almost only present on the upper half of Γ_1. The convection coefficient, meanwhile, depends on the wind velocity v_∞ [m.s^{-1}], as detailed in [27] and used in [17]:

$$v_\infty(t) = \cos(\omega_t \cdot t) + v_{10},$$
$$h_{\infty,1}(y,t) = h_{10} + h_{11} \cdot \frac{v_\infty}{v_0} \cdot \left(\frac{y}{y_0}\right)^\beta.$$

with h_{10} and h_{11} [W.m^{-2}.K^{-1}] surface coefficients, whose values are provided in Table 2. Then, $v_{10} = 1.5$ m.s^{-1} is the mean wind velocity, $\beta = 0.32$ the velocity variation coefficient, and $v_0 = 1$ m.s^{-1}, $y_0 = 65.33$ m are reference quantities.

For the boundary Γ_3, the temperature is held constant at $T_{\infty,3} = 15$ °C, no heat flux is applied, and the convection coefficient is defined as in [28], with a spatially varying profile:

$$h_{\infty,3}(y,t) = h_{20} + \left(h_{21} - h_{20}\right) \cdot \sin\left(\frac{\pi \cdot y}{H}\right).$$

where h_{20} and h_{21} [W.m^{-2}.K^{-1}] are surface coefficients, with their values provided in Table 2.

Finally, the initial temperature is set to $T_0 = 15$ °C throughout the entire domain Ω, and the simulation is run from $t_\text{i} = 0$ s to $t_\text{f} = 86,400$ s, corresponding to a full day.

The problem is then dimension changed over the spatial domain $\Omega = [0,1] \times [0,1]$ and the temporal domain $\Omega_t = [0,1]$, following the procedure described in Section 2.3. Once again, the superscript $\star$ is omitted here for the sake of clarity. In this context, the nondimensionalization coefficients T_ref and δT are chosen so as to ensure that the resulting values remain in $[0,1]$:

$$T_\text{ref} = \min_{j\in\{1,3\}} \min_{y,t}\Big(T_{\infty,j}(y,t)\Big), \qquad \delta T = \max_{y,t}\left(\frac{q_{\infty,1}(y,t)}{h_{\infty,1}(y,t)}\right) + T_\text{ref}.$$

giving $T_\text{ref} = 5$ °C and $\delta T = 35.5$ K.

In the end, the applied boundary conditions are illustrated in Fig. 7(a) and (b), while the results of the numerical model for two instants are presented in Fig. 7(c) and (d), where the shape of the interface in the dimensionless domain can be observed.

For this second validation, only the distribution of the error ϵ_2 is plotted in Fig. 8 for different spatial mesh refinement. The dimensionless time step is fixed at $\Delta t = 2.3 \cdot 10^{-3}$. The numerical model is first evaluated using a coarse mesh with $N = N_x = N_y = 30$ nodes in each spatial direction. As shown in Fig. 8(a), the magnitude of the error remains relatively small given the coarseness of the mesh, with a maximum value around 0.5%. These maximum errors are primarily located near the corners and close to the interface, which can already be partially distinguished. When refining the mesh to $N = 100$, as illustrated in Fig. 8(b), the maximum error decreases to below 0.1%. The spatial distribution of the error reveals several distinct regions of concentration.

First, around the interface, which is now clearly identified, with higher errors concentrated in the upper part. This corresponds to areas where the gradients are the steepest, as seen in Fig. 7(c) and (d).

Then, at the corners of the boundaryΓ_3 these points lie at the interface between two types of boundary conditions, which are treated in the developed model as a combination of both. However, the way the FEM model in `Matlab` handles such points differs. Specifically, the `applyBoundaryCondition` function assigns a single boundary condition to each node, and in cases where multiple conditions are applied to the same node, only the last one specified is retained [29]. Therefore, the discrepancy observed between the two models is entirely expected, as they are not solving the same boundary value problem at those corner points.

Thirdly, mid-height along the boundary Γ_1, where the applied flux $q_{\infty,1}$ exhibits strong spatial variation.

Last point, at the intersections between the interface and the boundaries Γ_2 and Γ_4, where the coupling between boundary and interface conditions likely leads to localized numerical discrepancies. Moreover, at this location, the boundary condition equations and the interface equations are combined. Furthermore, taking into account that the reference solution is subsequently interpolated onto the regular grid of the model, it becomes clear that identifying the exact source of discrepancies is not straightforward.

5. Application to optimal interface design in a realistic case

As buildings account for nearly 30% of global energy use [30], improving their thermal performance remains a key objective in energy efficiency strategies. Significant efforts have thus been devoted to the modeling of heat transfer through building envelopes [31,32], with the aim of supporting innovative design approaches [33]. While many studies have addressed global design parameters such as orientation and shape [34], fewer have focused on the detailed design of internal interfaces. In this section, we apply our method to a realistic case to investigate how optimizing interface morphology at the material scale can contribute to improved thermal performance.

5.1. Description

The case study considers a south-oriented facade of a building located in Nice, France. The wall has a height of $H = 3$ m and a width of $L = 40$ cm and is composed of two materials distributed as shown in Fig. 9 and with the properties in the Table 1 below. The two materials are separated by the interface defined in Eq. (26), which has already been used by [35] in the context of facade design. Given that $d_1 = 0.2$ m, this configuration corresponds to a highly efficient wall in the context of current French energy regulations [36], with an equivalent one-dimensional thermal resistance of R = 5.1 m^2.K.W^{-1} in the case where $p_0 = 0$.

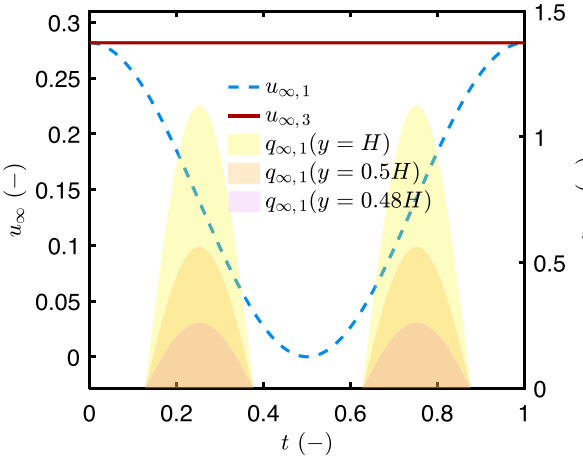

(a) *Boundary values and flux*

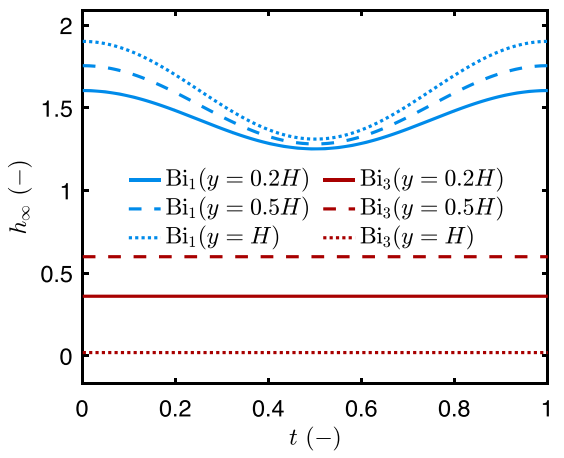

(b) *Biot numbers*

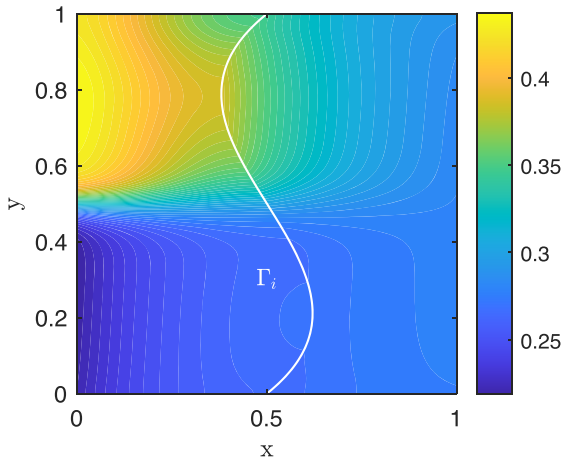

(c) $t = 0.33$

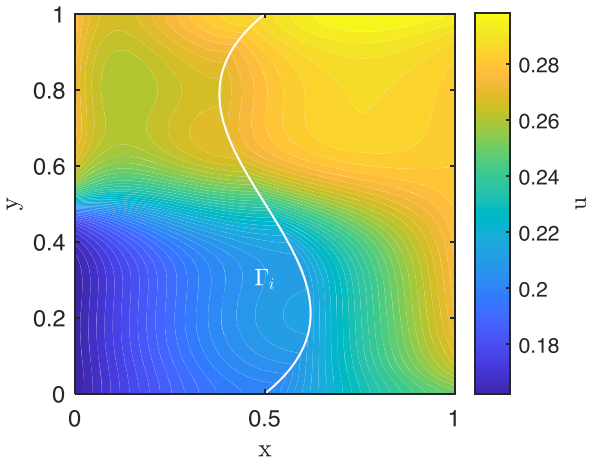

(d) $t = 0.66$

Fig. 7. Time evolution of boundary conditions (a) and (b), and results of value fields obtained with the numerical model (c) and (d).

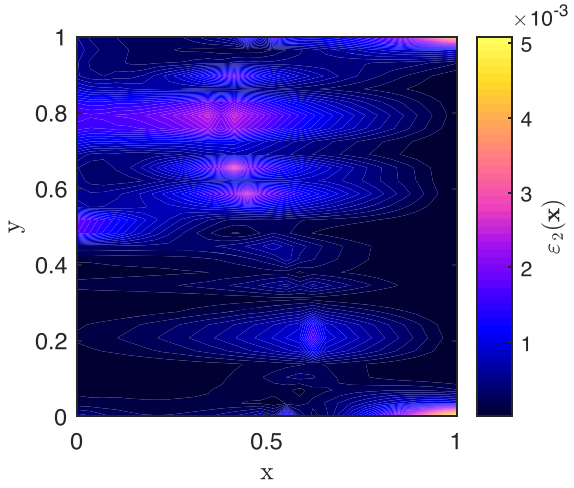

(a) $N = 30$

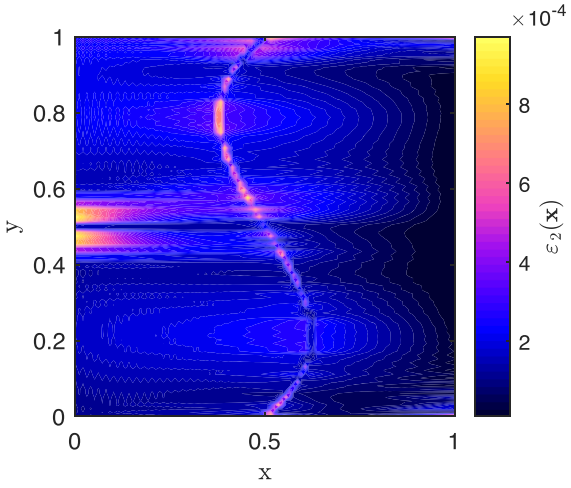

(b) $N = 100$

Fig. 8. L^2 error distribution according to different mesh refinement ($N = N_x = N_y$).

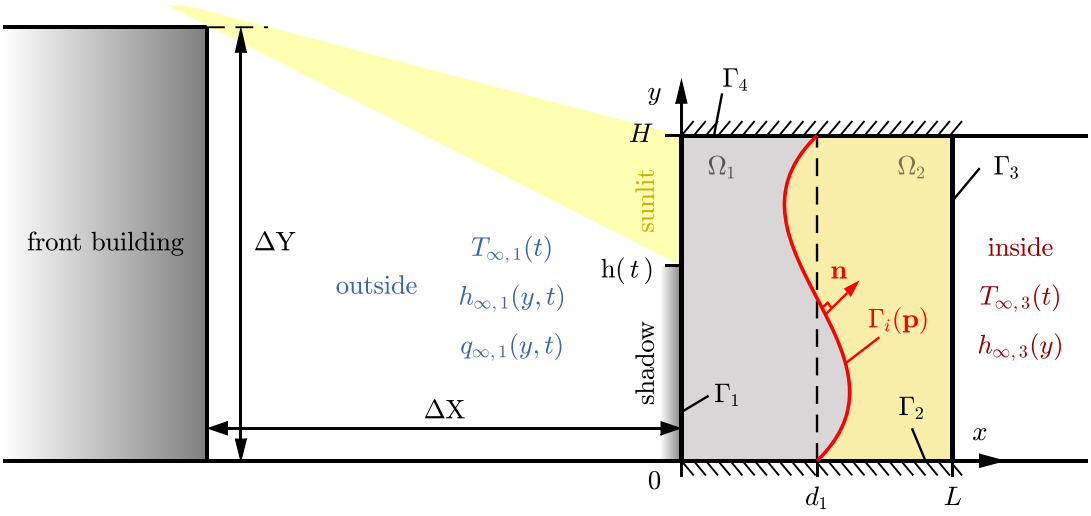

Fig. 9. Illustration of the urban street canyon configuration considered in the study.

The boundary conditions applied to the wall are identical to those used in the second validation case: ROBIN conditions are imposed on the external surface Γ_1 and on the internal surface Γ_3, while NEUMANN conditions are applied to the bottom and top boundaries Γ_3 and Γ_4. The expressions of the convective heat transfer coefficients remain unchanged, with the corresponding numerical values reported in Table 2. Here, wind velocity v_∞ varies based on meteorological data.

The outdoor temperature $T_{\infty,1}$ also follows time-dependent weather data. The indoor temperature $T_{\infty,3}$ is modeled as a function of the outdoor temperature, representing the thermal response of a conditioned indoor environment equipped with heating and cooling systems:

$$T_{\infty,3}(t) = \max\left(T^{\mathrm{w}}_{\mathrm{set}},\ \min\left(T^{\mathrm{s}}_{\mathrm{set}},\ T^{\mathrm{w}}_{\mathrm{set}} + \frac{T_{\infty,1}(t) - T_{\mathrm{heat}}}{T_{\mathrm{cool}} - T_{\mathrm{heat}}} \cdot \left(T^{\mathrm{s}}_{\mathrm{set}} - T^{\mathrm{w}}_{\mathrm{set}}\right)\right)\right)$$

The regulation is based on a setpoint logic using seasonal thresholds: $T^{\mathrm{w}}_{\mathrm{set}} = 19$ °C and $T^{\mathrm{s}}_{\mathrm{set}} = 24$ °C denote the indoor heating and cooling setpoint temperatures, respectively, while $T_{\mathrm{heat}} = 17$ °C and $T_{\mathrm{cool}} = 27$ °C are the corresponding outdoor threshold temperatures for the activation of heating and cooling systems.

The facade is located in an urban canyon setting, facing another building with a height $\Delta Y = 4$ m situated at a distance $\Delta X = 3$ m. This configuration leads to a time-dependent shadow on the facade due to the trajectory of the sun. The shadow height, denoted $h(t)$, is derived from a sunlit area ratio as described in [17], and calculated using a pixel-counting technique detailed in [37], which has already been implemented in building simulation tools such as `Domus` [38]. Consequently, the incident shortwave radiation flux $q_{\infty,1}$ on the exterior surface varies both temporally and spatially according to the following relation:

$$q_{\infty,1}(y,t) = \alpha \cdot \left(q^{\mathrm{dr}}_{\infty}(t) \cdot \chi(y,t) + q^{\mathrm{df}}_{\infty}(t) + q^{\mathrm{rf}}_{\infty}(t)\right)$$

with α [−] the wall absorptivity set to 0.7, $\chi(y,t)$ is a Boolean function indicating whether the coordinate y lies in the shaded or sunlit zone, and the terms $q^{\mathrm{dr}}_{\infty}(t)$, $q^{\mathrm{df}}_{\infty}(t)$, and $q^{\mathrm{dr}}_{\infty}(t)$ correspond respectively to the direct, diffuse, and reflected radiative fluxes derived from meteorological data.

Meteorological conditions are obtained from `Meteonorm` [39], and are used to define the boundary conditions shown in Fig. 10. These highlight the uneven distribution of radiative flux along the facade height Fig. 10(a), due to the street canyon configuration. In particular, direct radiation is only present on the upper part of the wall during winter, then extends over a larger surface in summer when the sun is higher in the sky. The lower quarter of the facade never receives any direct flux, as can be seen from the shadow height in Fig. 10(b). As a result, its magnitude never reaches that at mid-height or near the top of the facade. Fig. 10(c) shows that the climate in Nice generally leads to heating needs from October to June and cooling needs from July to September. External convection, Fig. 10(d), exhibits strong temporal variations, particularly in the upper part of the facade. For instance, daily values can range from 5 to over 30 $\mathrm{W.m^{-2}.K^{-1}}$. This highlights the importance of accounting for time-dependent convective effects, rather than assuming constant values as is often done.

For the entire study, simulations are performed over a one-year period, ($t_{\mathrm{f}} = 365$ d) using a time step of $\Delta t = 30$ s. Meteorological data, originally available every 6 min, are resampled at this time resolution using linear interpolation. The spatial domain is discretized with $N_x = N_y = 100$ nodes in each direction.

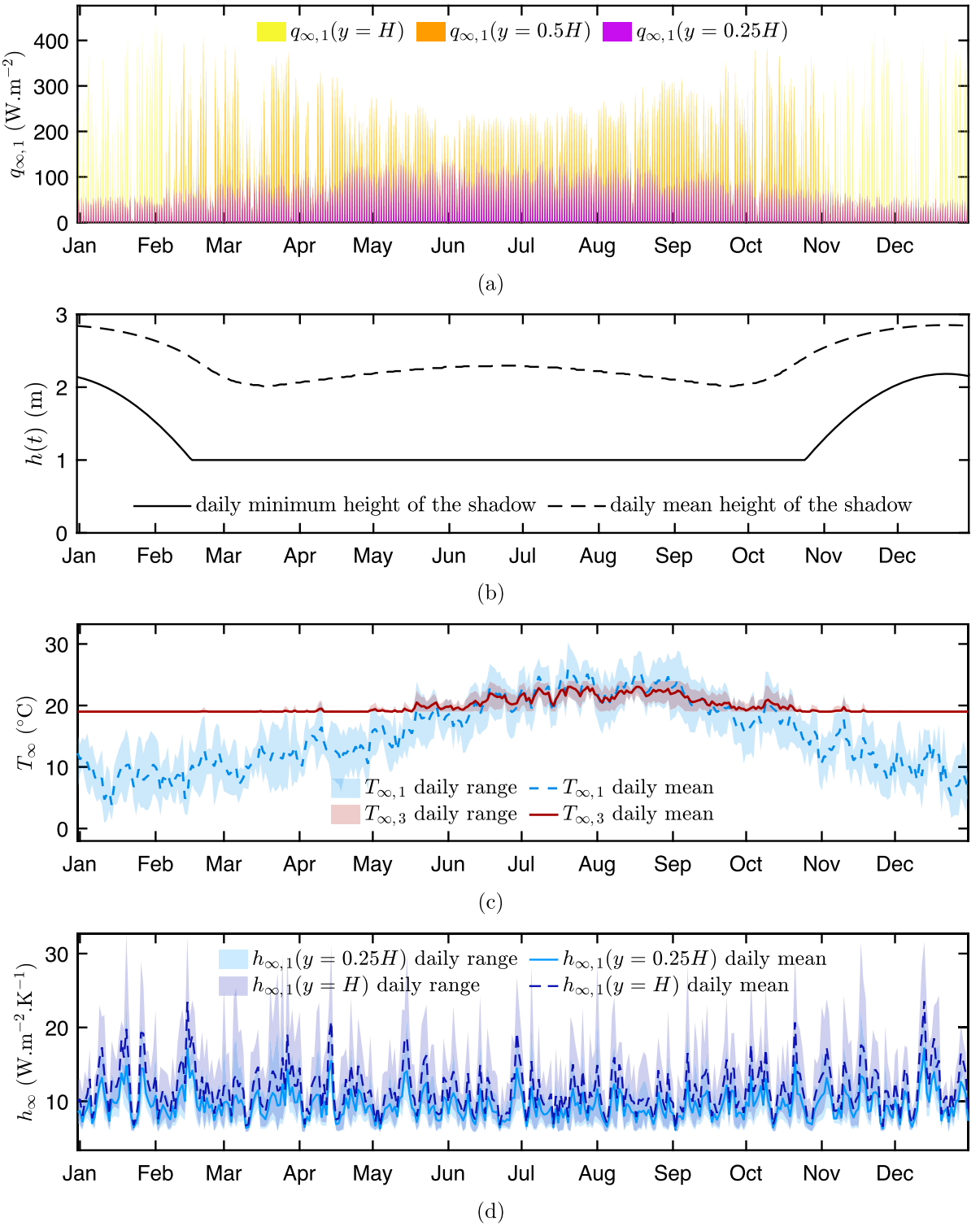

Fig. 10. Time variations of external incident short-wave radiative flux on the facade (a), shadow height on the facade (b), outdoor and indoor air temperatures (c), and external convective heat transfer coefficients (d).

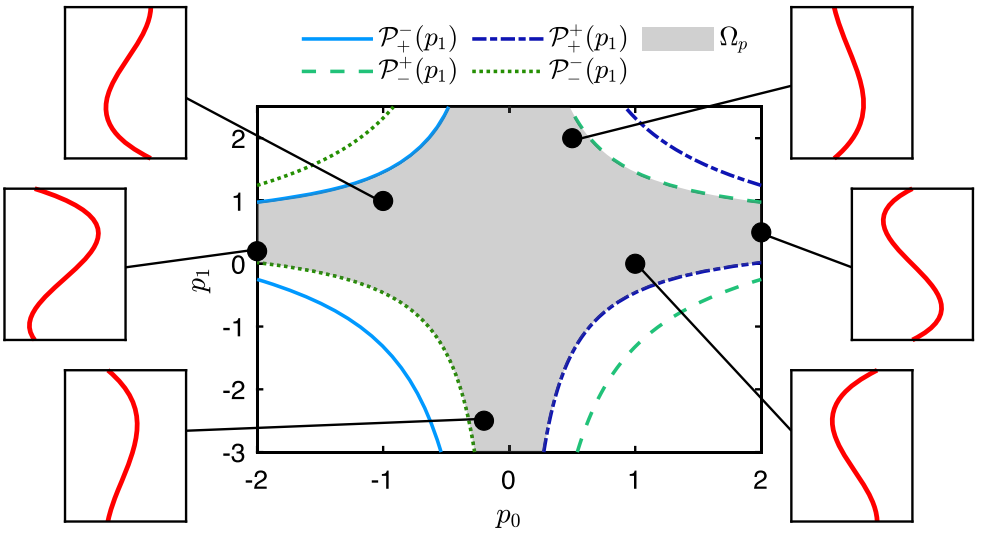

Fig. 11. Illustration of the research domain Ω_p with some interface examples.

5.2. Design performance assessment

The objective is to improve the wall energy efficiency by finding the optimal parametric coefficients $\mathbf{p}^\star$ of the interface function $\gamma(\mathbf{x}, \mathbf{p})$ Eq. (26) governing the Γ_i shape. Energy efficiency is defined regarding the heat flux $q(t)$ [W] on the inside boundary Γ_3:

$$q(t) = \int_0^H -\lambda(\mathbf{x}) \cdot \frac{\partial T}{\partial x} \, \mathrm{d}y,$$

Numerically, the surface heat flux $\varphi(y,t)$ [W.m^{-2}] is first approximated to second-order accuracy, and then integrated along the height of the wall using the trapezoidal rule:

$$\varphi_i^n = \frac{\lambda_{N_x\, i}}{\Delta x}\left(-\frac{3}{2}\, T^n_{N_x\, i} + 2\, T^n_{N_x-1\, i} - \frac{1}{2}\, T^n_{N_x-2\, i}\right),$$
$$q^n = \sum_{i=1}^{N_y-1} \frac{\Delta y}{2}\left(\varphi_i^n + \varphi_{i+1}^n\right).$$

Then, improving energy efficiency involves to minimizing a cost function C [J]. The optimization problem can thus be formulated as:

$$\mathbf{p}^\star = \arg \min_{\mathbf{p}\in\Omega_p} C.$$

Two cost functions, C_1 and C_2, are investigated in this study. The first one, C_1, corresponds to the integral of the absolute value of the heat flux $q(t)$ in Eq. (27), as the purpose is to minimize thermal exchanges between the inside and outside environments.

$$C_1 = \int_{t_\mathrm{i}}^{t_\mathrm{f}} |\, q(t)\,| \, \mathrm{d}t \;\approx\; \sum_{n=1}^{N_t-1} |\, q^n\,| \cdot \Delta t \tag{27}$$

In winter, the flux is typically negative (heat loss), and the objective is to reduce this loss. Conversely, in summer, the flux is positive (heat gain), and one seeks to limit it. Minimizing the absolute value of the flux over time thus captures the dual objective in both heating and cooling conditions.

The second cost function, C_2, is based on the *net consumed work*, comparing the wall as a thermal engine system, described in [40]. In this case, the heat flux is weighted by the ratio of outside to inside temperatures, reflecting the potential for mechanical work according to the second law of thermodynamics in Eq. (28).

$$C_2 = \int_{t_\mathrm{i}}^{t_\mathrm{f}} w(t) \, \mathrm{d}t \;\approx\; \sum_{n=1}^{N_t-1} w^n \cdot \Delta t \tag{28}$$

with: $w(t) = q(t)\left(\dfrac{T_{\infty,1}(t)}{T_{\infty,3}(t)} - 1\right)$.

Depending on the sign of the heat flux $q(t)$ and the temperature difference $(T_{\infty,1}(t) - T_{\infty,3}(t))$, expressed in [K], the wall may either consume or produce useful energy. For instance, if the wall extracts heat from the indoor environment while the outside air

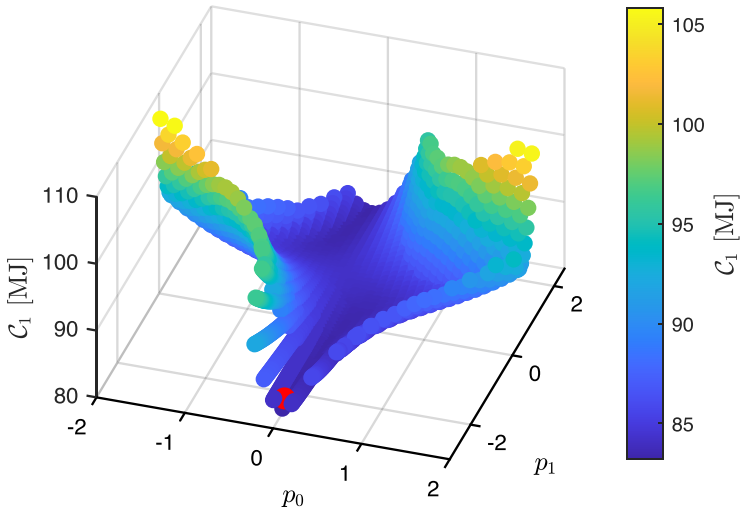

(a) *Cost function* $\mathcal{C}_1$

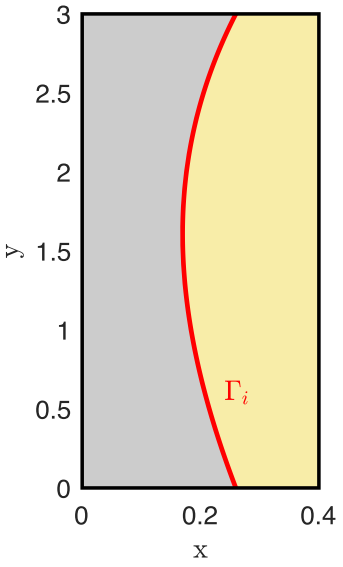

(b) $\mathbf{p}_1^\star = (0.11, -2.9)$

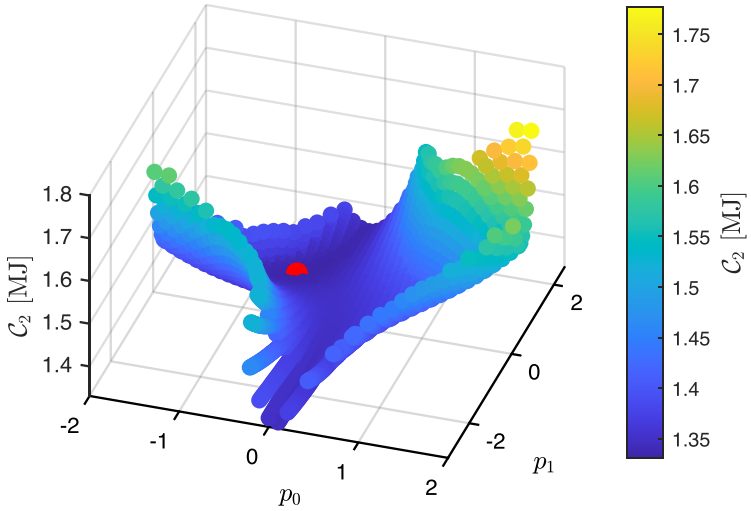

(c) *Cost function* $\mathcal{C}_2$

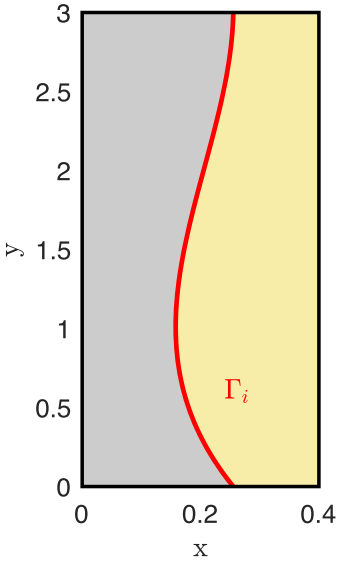

(d) $\mathbf{p}_2^\star = (-0.59, 1)$

Fig. 12. Illustration of the results of the exhaustive search (a) and (c), and of the optimal interfaces found (b) and (d).

is warmer, it leads to a net energy production, represented by a negative work $w(t)$ [W], which contributes to reducing $\mathcal{C}_2$. This formulation enables the identification of transient, energetically favorable regimes that are not captured by the first criterion. In contrast, $\mathcal{C}_1$ treats all heat exchanges uniformly and simply seeks to reduce their integrated magnitude.

5.3. Optimization strategy

To determine the optimal parameters $\mathbf{p}^\star$, an exhaustive search is conducted. It consists in performing N_p independent simulations, each corresponding to a parameter pair (p_0, p_1) within the following search domain Ω_p:

$$\Omega_p = \left\{ \mathbf{p} \in \mathbb{R}^2 \;\middle|\; \delta l \leq \hat{\gamma}(\mathbf{x}, \mathbf{p}) \leq L + \delta l,\ \mathbf{x} \in \Omega \right\}$$

Here, $\hat{\gamma}(\mathbf{x}, \mathbf{p})$ refers to the interface function Eq. (29) incorporating a volume constraint, ensuring that the interface Γ_i only produces shapes which preserve volumes of concrete Ω_1 and insulation Ω_2 equal to the case of a flat interface at d_1. The function $\hat{\gamma}(\mathbf{x}, \mathbf{p})$ is

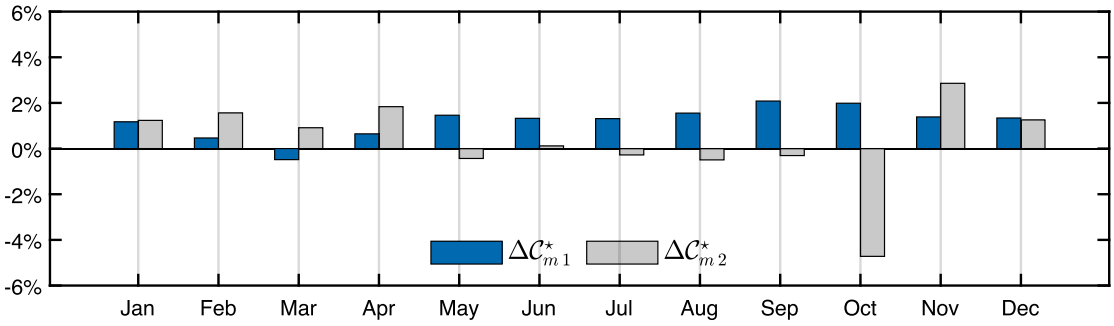

Fig. 13. Illustration of monthly improvements in $C_1^{\star}$ and $C_2^{\star}$ cost functions values.

Table 3
Direction and location of the concavity according to $(p_0,\ p_1)$.

	$p_0 < 0$	$p_0 > 0$
$p_1 < 0.5$	Concavity at the top opening to the right	Concavity at the top opening to the left
$p_1 > 0.5$	Concavity at the bottom opening to the left	Concavity at the bottom opening to the right

determined using the method in [41], by introducing a constant term into $\gamma(\mathbf{x}, t)$ Eq. (26) that enforces the volume constraint, as detailed in Appendix A. This leads to the following function:

$$\widehat{\gamma}(\mathbf{x}, \mathbf{p}) = x - \left[d_1 + p_0 \frac{y}{H} \left(\frac{y}{H} - p_1 \right) \left(\frac{y}{H} - 1 \right) - \frac{p_0 \,(2\, p_1 - 1)}{12} \right] \tag{29}$$

It is worth noting that the inclusion of this constraint leads to interfaces with identical anchor points at the top and bottom of the wall. Moreover, the case $p_0 = 0$ corresponds to a flat interface, which serves as the reference configuration.

Furthermore, a spatial constraint is added restricting the shape of Γ_i to remain within the wall domain Ω, with a safety margin δl [m] computed to ensure a minimum width of four mesh cells between boundary and interface. This margin is necessary for constructing the boundary conditions used in the numerical scheme described in Section 3.3. The incorporation of these constraints in the construction of the domain Ω_p is fully detailed in Appendix A.

In the following, the search domain is restricted to the intervals $p_0 \in [-2, 2]$ and $p_1 \in [-3, 2.5]$, which are discretized into 46×46 values. After applying the space constraints, this results in $N_p = 1055$ couples $(p_0,\ p_1)$ within the domain shown in Fig. 11, which is bounded by the curves $\mathcal{P}_+^-(p_1)$, $\mathcal{P}_+^+(p_1)$, $\mathcal{P}_-^+(p_1)$ and $\mathcal{P}_-^-(p_1)$ representing the spatial constraints detailed in the Appendix A. Regarding the shape of the interface, it is observed that p_0 controls its amplitude, while p_1 determines the location of the inflection point. When p_1 is close to 0.5, the interface exhibits two concavities; as p_1 moves away from this value, a single dominant concavity emerges. The location of this concavity then depends on the specific position within the domain. Table 3 below illustrates how the position of the concavity varies with different $(p_0,\ p_1)$ values.

5.4. Results

The optimization procedure is carried out as detailed in Sections 5.1 to 5.3. The annual results for the cost functionals C_1 and C_2 are displayed in the scatter plots of Fig. 12(a) and (c). These distributions form a surface with a similar overall shape for both functionals, where the point minimizing each functional is highlighted in red. Notably, the optimized parameter $\mathbf{p}^{\star}$ differ between C_1 and C_2, highlight the different objectives emphasised by each indicator.

Thus, for C_1, the optimized interface corresponds to the parameter set $\mathbf{p}_1^{\star} = (0.11,\ -2.9)$, giving the shape shown in Fig. 12(b). This configuration results in a shape with a concavity centred along the wall and directed outwards. In contrast, the optimized interface for C_2, shown in Fig. 12(d), is obtained for $\mathbf{p}_2^{\star} = (-0.59,\ 1)$, which produces a concavity located near the bottom, also facing outwards. Consequently, C_2 favours a wall configuration with greater insulation in the lower part compared to the upper part, which tends to increase the impact of solar gains over the year, as these are predominantly concentrated in the upper part of the facade as illustrated in Fig. 10(a). In contrast, C_1 promotes a design with greater insulation in the centre of the wall. This configuration still allows the winter solar gains to be exploited in the upper region, but reduces their effect in summer because the solar flux is better distributed across the facade.

Finally, from a quantitative perspective, the relative improvements compared to the reference configuration with flat interface remain modest, with $\Delta C_1^{\star} = 1.22\%$ and $\Delta C_2^{\star} = 1.55\%$ respectively.

To better capture seasonal dynamics that are obscured by annual integration, the monthly relative improvements compared with the reference configuration $\Delta C^{\star}_{m\,1}$ and $\Delta C^{\star}_{m\,2}$ are analyzed. Fig. 13 presents these monthly improvements for each cost functional.

First, it is observed that the values remain within a moderate range (between -5% and $+4\%$), although different trends can be identified depending on the cost functions. Functional $C_1^{\star}$ exhibits an improvement for all months of the year except March, whereas $C_2^{\star}$ shows a nearly equal number of months with improved and degraded performance. During the winter period, the improvements

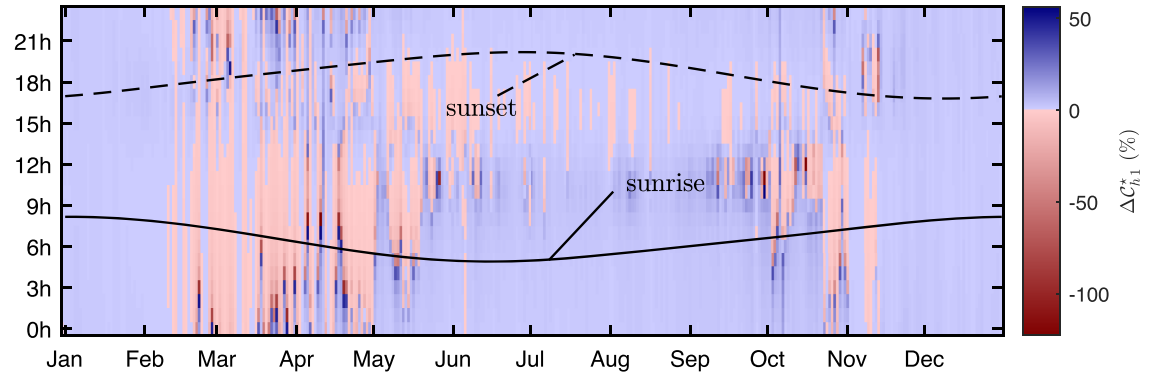

(a) *Hourly improvement of* $\mathcal{C}^{\star}_{h\,1}$

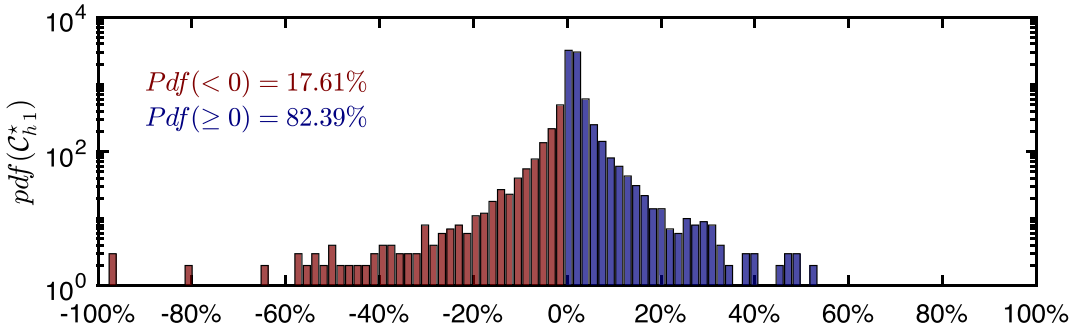

(b) *Probability density function of* $\mathcal{C}^{\star}_{h\,1}$.

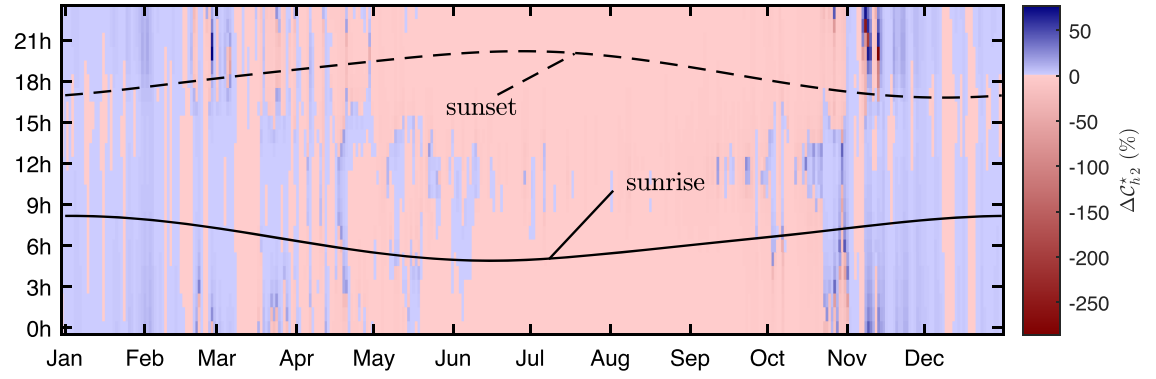

(c) *Hourly improvement of* $\mathcal{C}^{\star}_{h\,2}$

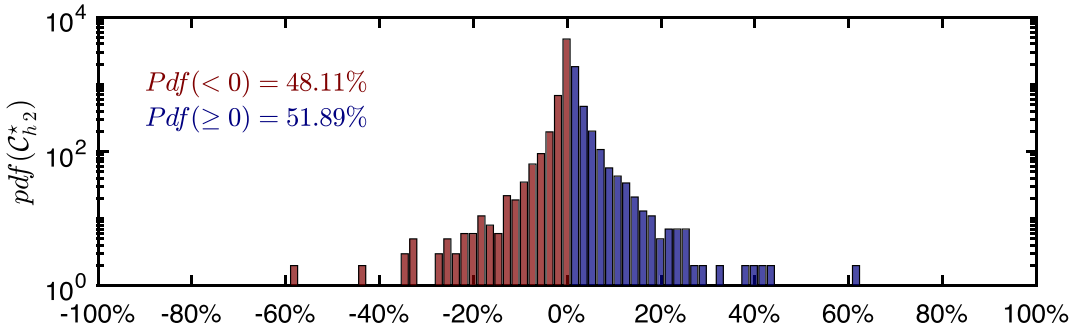

(d) *Probability density function of* $\mathcal{C}^{\star}_{h\,2}$.

Fig. 14. Illustration of hourly improvements (a) and (c) and their probability density function (b) and (d).

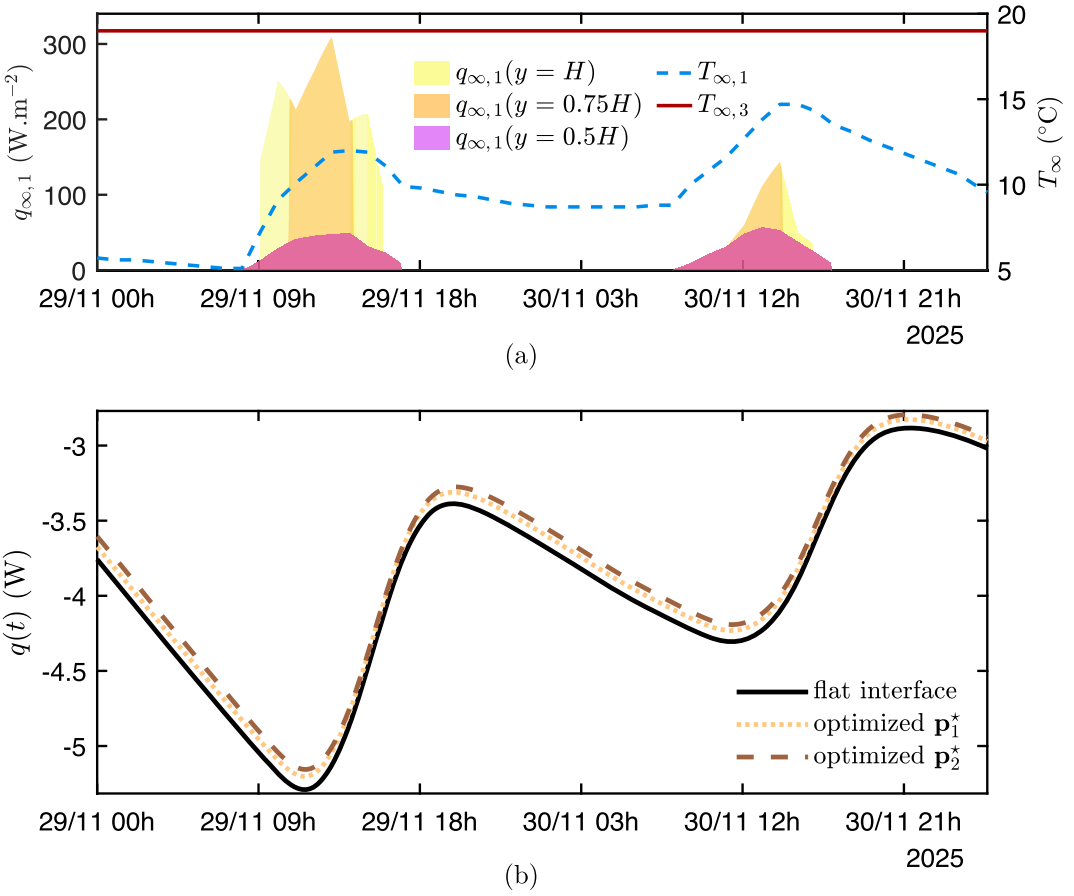

Fig. 15. Evolution of the internal flux for the two optimised cases found in comparison with the reference case with flat interface (a) over two winter days. Boundary conditions experienced by the facade (b).

associated with $C_2^\star$ are more pronounced than those of $C_1^\star$, which may be attributed to a reduced amount of insulation in the upper part of the wall, allowing greater solar heat gains. Conversely, during the summer period, $C_1^\star$ outperforms $C_2^\star$ due to its enhanced insulation in the upper half of the wall. In contrast, $C_2^\star$ leads to a deterioration in wall performance during this season, likely due to insufficient insulation in the upper section.

The time scale is then reduced again to examine the hourly behaviour of the two cost functions. Fig. 14(a) and (c) illustrate the performance variations throughout the day (vertical axis) over the course of the year (horizontal axis), with hourly improvements represented by blue gradients and deteriorations by red gradients ($\Delta C_{h1}^\star$ and $\Delta C_{h2}^\star$).

As previously noted, cost function $C_1^\star$ leads to improved performance for a large part of the year, with dynamic gains reaching over 50%. During winter, the wall performance consistently surpasses that of the reference case, regardless of the time of day. Degraded situations primarily occur during the mid-season, at night or in the early morning, when the outdoor temperature is lower than the indoor temperature and no solar radiation is present. During this period, improvements appear in the late afternoon, when the impact of solar gains becomes noticeable on the inside surface of the wall. In summer, the opposite behavior is observed: performance degradation tends to occur in the late afternoon, primarily due to solar radiation. This analysis is complemented by the probability density function (pdf) shown in Fig. 14(b), which illustrates the distribution of $\Delta C_{h1}^\star$. Although cases with performance degradation exceeding 100% are observed, they are extremely rare. Moreover, improvement cases account for more than 82% of the total.

In contrast, the results for $C_2^\star$ Fig. 14(c) show markedly different behavior: overall performance is improved during winter and degraded during summer. In mid-season, improvements are primarily observed around midday, which may correspond to situations where the heat flux is directed into the building while the outdoor temperature remains lower than the indoor temperature, resulting in a negative net consumed work ω. Finally, the performance assessed with $C_2^\star$ shows improvement in approximately 52% of cases, and degradations greater than 50% are nearly nonexistent (Fig. 14(d)), as is also the case for $C_1^\star$.
Ultimately, although the annual and monthly improvements remain modest, it is worth noting that significant instantaneous improvements can be observed at the hourly scale, reaching up to 60%.

Finally, two days at the end of November are selected to plot Fig. 15(b) the evolution of the heat flux q reaching the inside surface of the building facade for the two optimized configurations, $\mathbf{p}_1^\star$ and $\mathbf{p}_2^\star$, as well as for the reference case. These situations correspond to improvement scenarios according to the objective functions Fig. 14(a) and (c). The results show that, for all cases considered, heat losses are strongly correlated with the variation of the outdoor temperature Fig. 15(a), with a thermal phase shift of several hours. Moreover, the difference between the reference case and the two optimized configurations remains small during the day but becomes more pronounced at night, when heat losses increase. This suggests that the material arrangement in the wall for both optimized cases enhances heat storage within the facade, thereby improving its overall energy performance. This reduction is slightly more pronounced for the facade corresponding to $\mathbf{p}_2^\star$ than for $\mathbf{p}_1^\star$.

6. Conclusion

In this paper, a novel two-dimensional transient diffusion model with a source term for composite domains has been presented. The model is based on the finite difference method using the explicit DuFort-Frankel scheme, chosen for its improved accuracy and computational efficiency. Interface treatment between subdomains is handled using the Ghost Fluid Method, originally developed for fluid dynamics simulations, which enables accurate resolution of interface problems on a structured Cartesian grid. Jump conditions in both value and flux are incorporated, with flux discontinuities approximated along the mesh axes only, an aspect that constitutes a distinctive feature of this model.

The model is validated in two steps. First, it was tested against an analytical solution (Section 4.1), which demonstrated both the accuracy and robustness of the scheme for various interface geometries. The model retains second-order accuracy in both time and space, consistent with the classical DuFort-Frankel scheme, indicating that the incorporation of interface equations does not compromise the numerical properties of the scheme. Additionally, error comparisons were made against two alternative finite difference models from the literature that also incorporate the Ghost Fluid Method–namely, an implicit Euler scheme and an Alternating Direction Implicit scheme. The results confirmed consistency among the models in accordance with their theoretical properties. In the second validation step (Section 4.2), the model was compared to a finite element code in order to assess its performance under a broader set of conditions and in a more realistic building thermal context. This comparison further confirmed the model reliability and effectiveness.

Finally, in Section 5, the model was applied to the optimization of interface shapes in a building wall composed of two materials and subject to spatially heterogeneous boundary conditions, representative of an urban canyon environment. Due to the computational efficiency of the model, a direct exhaustive search was performed. Optimal shapes were identified according to two distinct cost functions, resulting in two clearly differentiated solutions. Although the annual and monthly performance improvements were modest, the analysis at a finer temporal scale revealed that instantaneous gains could reach up to 60%, highlighting the importance of the temporal scale of observation in this type of problem.m.

Looking ahead, the simplicity of the interface representation via parametric functions is an aspect that could be further developed to enhance model flexibility. As for the application context, future work will focus on a more formal optimization framework for interface shape design in building walls, accompanied by a deeper physical analysis of the observed thermal phenomena.

Data availability

Data will be made available on request.

Acknowledgments

The authors would like to acknowledge the French National Research Agency (Agence Nationale de la Rcherche: ANR) for funding the TOPS project as part of the *JCJC CE-22 AAPG 2023 programme*.

Appendix A. Constraints application on the research domain of the realistic case study

Lets consider the initial interface function $\gamma(\mathbf{x}, \mathbf{p})$ Eq. (26), to which we add the term $\mathrm{A}(\mathbf{p})$ incorporating the volume constraint:

$$\widehat{\gamma}(\mathbf{x}, \mathbf{p}) = \gamma(\mathbf{x}, \mathbf{p}) + \mathrm{A}(\mathbf{p}),$$

Next, if we impose the volume conservation of the two subdomains Ω_1 and Ω_2, this is equivalent to setting the integral of the new interface function to zero for $x = d_1$:

$$\int_0^H \widehat{\gamma}(x = d_1,\, y,\, \mathbf{p})\, \mathrm{d}y = 0 \quad \Longrightarrow \quad \mathrm{A}(\mathbf{p}) = -\int_0^H \gamma(x = d_1,\, y,\, \mathbf{p})\, \mathrm{d}y,$$

this gives in detail:

$$\mathrm{A}(\mathbf{p}) = \int_0^H p_0\, \frac{y}{H} \left(\frac{y}{H} - p_1 \right) \left(\frac{y}{H} - 1 \right) \mathrm{d}y,$$

$$\mathrm{A}(\mathbf{p}) = \frac{p_0\,(2\,p_1 - 1)}{12}.$$

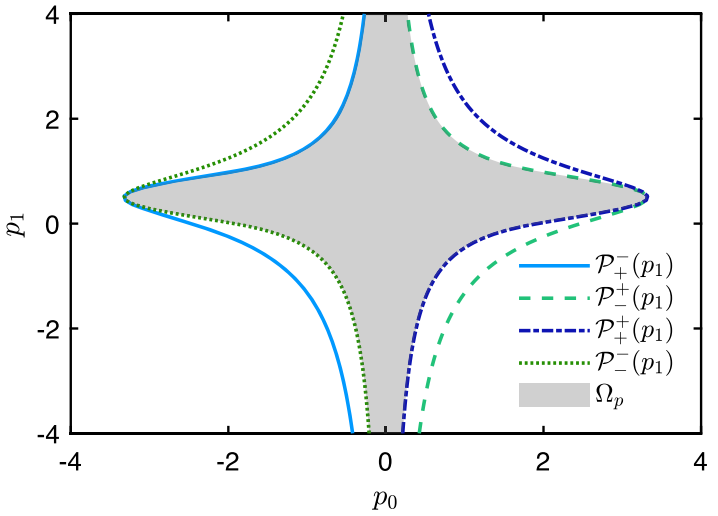

Fig. A.1. Illustration of the research area **p** with space constraints.

The second constraint further restricts the extent of $\hat{\gamma}(\mathbf{x}, \mathbf{p})$ so that it remains within the domain Ω, up to a margin δl:

$$\delta l \;\le\; L - \left[d_1 + p_0 \frac{y}{H}\left(\frac{y}{H} - p_1\right)\left(\frac{y}{H} - 1\right) - \frac{p_0\,(2\,p_1 - 1)}{12} \right] \;\le\; L - \delta l \tag{A.1}$$

which can be reformulated as:

$$-d_1 + \delta l \;\le\; p_0 \cdot \gamma_p(y, p_1) \;\le\; L - d_1 - \delta l$$

with:

$$\gamma_p(y, p_1) = \frac{y}{H}\left(\frac{y}{H} - p_1\right)\left(\frac{y}{H} - 1\right) - \frac{2\,p_1 - 1}{12}$$

We then need to distinguish cases based on the sign of p_0:
First, in the case where $p_0 > 0$, the following inequality must be satisfied:

$$p_0 \;<\; \min\left(\mathcal{P}_+^+(p_1)\,,\; \mathcal{P}_-^+(p_1)\right) \tag{A.2}$$

with: $\mathcal{P}_+^+(p_1) = \dfrac{L - d_1 - \delta l}{\gamma_p^+(p_1)}, \qquad \mathcal{P}_-^+(p_1) = \dfrac{-d_1 + \delta l}{\gamma_p^-(p_1)}.$

The inequality Eq. (A.2) reflects the fact that we seek the extrema of the function $\gamma_p(y, p_1)$ over the interval $[0, H]$ in order to verify whether each of them satisfies Eq. (A.1). The extrema are identified using the conditional functions $\gamma_p^+(p_1)$ and $\gamma_p^-(p_1)$, which evaluate $\gamma_p(y, p_1)$ at the point where its derivative is zero, provided this critical point lies within $[0, H]$; otherwise, the value $\gamma_p(y = 0, p_1)$ is used. The value $\gamma_p(y = H, p_1)$ could also be used instead, but this makes no difference since $\gamma_p(y = 0, p_1) = \gamma_p(y = H, p_1)$.

$$\gamma_p^+(p_1) = \begin{cases} \gamma_p\big(\, y^+(p_1), p_1 \,\big), & \text{if } y^+(p_1) \in [0, H], \\ \gamma_p\big(\, y = 0, p_1 \,\big), & \text{otherwise.} \end{cases}$$

with: $y^+(p_1) = \arg\min_{y \in [0,H]} \gamma_p(\, y, p_1\,) = \dfrac{H}{3}\left(1 + p_1 - \sqrt{p_1^2 - p_1 + 1}\right),$

$$\gamma_p^-(p_1) = \begin{cases} \gamma_p\big(\, y^-(p_1), p_1 \,\big), & \text{if } y^-(p_1) \in [0, H], \\ \gamma_p\big(\, y = 0, p_1 \,\big), & \text{otherwise.} \end{cases}$$

with: $y^-(p_1) = \arg\max_{y \in [0,H]} \gamma_p(\, y, p_1\,) = \dfrac{H}{3}\left(1 + p_1 + \sqrt{p_1^2 - p_1 + 1}\right).$

Next, in the case where $p_0 < 0$, we proceed in an analogous manner:

$$p_0 \;<\; \max\left(\mathcal{P}_+^-(p_1)\,,\; \mathcal{P}_-^-(p_1)\right) \tag{A.3}$$

with: $\mathcal{P}_+^-(p_1) = \dfrac{L - d_1 - \delta l}{\gamma_p^-(p_1)}, \qquad \mathcal{P}_-^+(p_1) = \dfrac{-d_1 + \delta l}{\gamma_p^+(p_1)}.$

Finally, the case $p_0 = 0$ corresponds to a flat interface passing through d_1, which therefore always satisfies the constraints.
This defines the search domain Ω_p, illustrated in Fig. A.1 below for $p_0 \in [-4, 4]$, which forms a connected space.

References

[1] S. Gasparin, J. Berger, D. Dutykh, N. Mendes, et al., An adaptive simulation of nonlinear heat and moisture transfer as a boundary value problem, Int. J. Therm. Sci. 133 (2018) 120–139. arXiv:1902.09951[cs], https://doi.org/10.1016/j.ijthermalsci.2018.07.013

[2] R.I. Hickson, S.I. Barry, G.N. Mercer, H.S. Sidhu, et al., Finite difference schemes for multilayer diffusion, Math. Comput. Model. 54 (1) (2011) 210–220. https://doi.org/10.1016/j.mcm.2011.02.003

[3] J. Kośny, E. Kossecka, Multi-dimensional heat transfer through complex building envelope assemblies in hourly energy simulation programs, Energy Build. 34 (5) (2002) 445–454. https://doi.org/10.1016/S0378-7788(01)00122-0

[4] K. Regenauer-Lieb, D.A. Yuen, Modeling shear zones in geological and planetary sciences: solid- and fluid-thermal-mechanical approaches, Earth Sci. Rev. 63 (3) (2003) 295–349. https://doi.org/10.1016/S0012-8252(03)00038-2

[5] J.D. Clayton, Mesoscale models of interface mechanics in crystalline solids: a review, J. Mater. Sci. 53 (8) (2018) 5515–5545. https://doi.org/10.1007/s10853-017-1596-2. https://doi.org/10.1007/s10853-017-1596-2

[6] P. Sun, Modeling studies and efficient numerical methods for proton exchange membrane fuel cell, Comput. Methods Appl. Mech. Eng. 200 (47) (2011) 3324–3340. https://doi.org/10.1016/j.cma.2011.08.007

[7] G. Marck, Y. Privat, On some shape and topology optimization problems in conductive and convective heat transfers, in: M. Papadrakakis, M.G. Karlaftis, N.D. Lagaros (Eds.), OPT-I Conference Proceedings, Kos Island, Greece, 2014, pp. 1640–1657. https://hal.science/hal-01054711.

[8] L.C. Sousa, C.F. Castro, C.C. António, H. Sousa, Topology optimisation of masonry units from the thermal point of view using a genetic algorithm, Constr. Build. Mater. 25 (5) (2011) 2254–2262. https://doi.org/10.1016/j.conbuildmat.2010.11.010

[9] M. Bruggi, A. Taliercio, Design of masonry blocks with enhanced thermomechanical performances by topology optimization, Constr. Build. Mater. 48 (2013) 424–433. https://doi.org/10.1016/j.conbuildmat.2013.07.023

[10] G. Vantyghem, V. Boel, M. Steeman, W. De Corte, Multi-material topology optimization involving simultaneous structural and thermal analyses, Struct. Multidiscip. Optim. 59 (3) (2019) 731–743. https://doi.org/10.1007/s00158-018-2095-z

[11] O. Sigmund, K. Maute, Topology optimization approaches, Struct. Multidiscip. Optim. 48 (6) (2013) 1031–1055. https://doi.org/10.1007/s00158-013-0978-6

[12] R.P. Fedkiw, T. Aslam, B. Merriman, S. Osher, A non-oscillatory eulerian approach to interfaces in multimaterial flows (the ghost fluid method), J. Comput. Phys. 152 (2) (1999) 457–492. https://doi.org/10.1006/jcph.1999.6236

[13] X.-D. Liu, R.P. Fedkiw, M. Kang, et al., A boundary condition capturing method for poisson's equation on irregular domains, J. Comput. Phys. 160 (1) (2000) 151–178. https://doi.org/10.1006/jcph.2000.6444

[14] M.J. Geiss, J.L. Barrera, N. Boddeti, K. Maute, et al., A regularization scheme for explicit level-set XFEM topology optimization, Front. Mech. Eng. 14 (2) (2019) 153–170. https://doi.org/10.1007/s11465-019-0533-2

[15] S. Gasparin, J. Berger, D. Dutykh, N. Mendes, et al., Numerical schemes for the solution of non-linear moisture transfer in porous materials: Implicit or explicit?, 2017, arXiv:1701.07059 version: 2. http://arxiv.org/abs/1701.07059.

[16] J.M. Hobson, N. Wood, P.J. Mason, et al., A new finite-difference diffusion scheme, J. Comput. Phys. 125 (1) (1996) 16–25. https://doi.org/10.1006/jcph.1996.0076

[17] J. Berger, S. Gasparin, W. Mazuroski, N. Mendes, et al., An efficient two-dimensional heat transfer model for building envelopes, Numer. Heat Transf. a: Appl. 79 (3) (2020) 163–194. Publisher: Taylor & Francis https://doi.org/10.1080/10407782.2020.1836936

[18] S. Gasparin, J. Berger, D. Dutykh, N. Mendes, et al., An innovative method to determine optimum insulation thickness based on non-uniform adaptive moving grid, J. Braz. Soc. Mech. Sci. Eng. 41 (4) (2019) 173. https://doi.org/10.1007/s40430-019-1670-6

[19] R. Courant, K. Friedrichs, H. Lewy, et al., Über die partiellen differenzengleichungen der mathematischen physik, Math. Ann. 100 (1) (1928) 32–74. https://doi.org/10.1007/BF01448839

[20] C. Li, Z. Wei, G. Long, C. Campbell, S. Ashlyn, S. Zhao, et al., Alternating direction ghost-fluid methods for solving the heat equation with interfaces, Comput. Math. Appl. 80 (5) (2020) 714–732. https://doi.org/10.1016/j.camwa.2020.04.027

[21] Partial Differential Equation Toolbox, 2026, https://fr.mathworks.com/help/releases/R2024b/pde/index.html.

[22] interpolateSolution, 2026). https://fr.mathworks.com/help/releases/R2024b/pde/ug/pde.stationaryresults.interpolatesolution.html.

[23] P. Bigdelou, C. Liu, P. Tarey, P. Ramaprabhu, et al., An efficient ghost fluid method to remove overheating from material interfaces in compressible multi-medium flows, Comput. Fluids 233 (2022) 105250. https://doi.org/10.1016/j.compfluid.2021.105250

[24] R.P. Fedkiw, A. Marquina, B. Merriman, An isobaric fix for the overheating problem in multimaterial compressible flows, J. Comput. Phys. 148 (2) (1999) 545–578. https://doi.org/10.1006/jcph.1998.6129

[25] L. Xu, C. Feng, T. Liu, Practical techniques in ghost fluid method for compressible multi-medium flows, Commun. Comput. Phys. 20 (3) (2016) 619–659. https://www.cambridge.org/core/journals/communications-in-computational-physics/article/abs/practical-techniques-in-ghost-fluid-method-for-compressible-multimedium-flows/8CB42B84134ECC453F2908DA09D7CD52. https://doi.org/10.4208/cicp.190315.290316a

[26] Get Intel® oneAPI HPC Toolkit, 2026, https://www.intel.com/content/www/us/en/developer/tools/oneapi/hpc-toolkit-download.html.

[27] Z. Karashbayeva, S. Gasparin, J. Berger, et al., Optimisation of the insulation domain for heat transfer in building wall, in: 11th International Conference on Inverse Problems in Engineering: Theory and Practice (ICIPE 2024), Buzios, Brazil, 2024. https://hal.science/hal-04660099.

[28] G.H. dos Santos, N. Mendes, P.C. Philippi, et al., A building corner model for hygrothermal performance and mould growth risk analyses, Int. J. Heat Mass Transf. 52 (21) (2009) 4862–4872. https://doi.org/10.1016/j.ijheatmasstransfer.2009.05.026

[29] applyBoundaryCondition - Add boundary condition to PDEModel container - MATLAB, 2026. https://fr.mathworks.com/help/pde/ug/pde.pdemodel.applyboundarycondition.html.

[30] P. IEA, World energy outlook 2022, Paris, France: International Energy Agency (IEA), 2022.

[31] M. Woloszyn, C. Rode, Tools for performance simulation of heat, air and moisture conditions of whole buildings, Build. Simul. 1 (1) (2008) 5–24. https://doi.org/10.1007/s12273-008-8106-z

[32] N. Mendes, M. Chhay, J. Berger, D. Dutykh, et al., Numerical Methods for Diffusion Phenomena in Building Physics: A Practical Introduction, Springer International Publishing, Cham, Cham, 2019. http://link.springer.com/10.1007/978-3-030-31574-0. https://doi.org/10.1007/978-3-030-31574-0

[33] H.L. Gauch, C.F. Dunant, W. Hawkins, A. Cabrera Serrenho, et al., What really matters in multi-storey building design? a simultaneous sensitivity study of embodied carbon, construction cost, and operational energy, Appl. Energy 333 (2023) 120585. https://doi.org/10.1016/j.apenergy.2022.120585

[34] A. Ciardiello, F. Rosso, J. Dell'Olmo, V. Ciancio, M. Ferrero, F. Salata, et al., Multi-objective approach to the optimization of shape and envelope in building energy design, Appl. Energy 280 (2020) 115984. https://doi.org/10.1016/j.apenergy.2020.115984

[35] S. Alpar, J. Berger, W. Mazuroski, R. Belarbi, et al., Shape optimization of the energy efficiency of building retrofitted facade, Sol. Energy 271 (2024) 112437. https://doi.org/10.1016/j.solener.2024.112437

[36] Arrêté du 4 août 2021 relatif aux exigences de performance énergétique et environnementale des constructions de bâtiments en France métropolitaine et portant approbation de la méthode de calcul prévue à l'article R. 172-6 du code de la construction et de l'habitation - Légifrance, 2026. https://www.legifrance.gouv.fr/jorf/id/JORFTEXT000043936431?utm_source=chatgpt.com.

[37] N.L. Jones, D. P. Greenberg, K.B. Pratt, Fast computer graphics techniques for calculating direct solar radiation on complex building surfaces, J. Build. Perform. Simul. 5 (5) (2012) 300–312. Publisher: Taylor & Francis https://doi.org/10.1080/19401493.2011.582154

[38] R.A.P. de Almeida, R.C.L.F. Oliveira, N. Mendes, et al., Experimental validation and comparison of direct solar shading calculations within building energy simulation tools: polygon clipping and pixel counting techniques, Sol. Energy 158 (2017) 462–473. https://doi.org/10.1016/j.solener.2017.10.011

[39] Meteonorm, 2026. https://meteonorm.com/en/.

[40] F. Strub, J. Castaing-Lasvignottes, M. Strub, M. Pons, F. Monchoux, et al., Second law analysis of periodic heat conduction through a wall, Int. J. Therm. Sci. 44 (12) (2005) 1154–1160. https://linkinghub.elsevier.com/retrieve/pii/S1290072905002127. https://doi.org/10.1016/j.ijthermalsci.2005.09.004

[41] P. Blanchard, E. Brüning, Constrained minimisation problems (method of lagrange multipliers), in: P. Blanchard, E. Brüning (Eds.), Variational Methods in Mathematical Physics: a Unified Approach, Springer, Berlin, Heidelberg, 1992, pp. 63–76. https://doi.org/10.1007/978-3-642-82698-6_5